

Tangent Hyperbolic Non-Newtonian Radiative Bioconvection Nanofluid Flow from a Bi-Directional Stretching Surface with Electro-Magneto-Hydrodynamic, Joule Heating and Modified Diffusion Effects

¹J. Prakash, ^{*2}Dharmendra Tripathi, ³Nevzat Akkurt and ⁴O. Anwar Bég

¹Department of Mathematics, Avvaiyar Government College for Women, Karaikal – 609 602,

U.T of Puducherry, **India**. prakashjayavel@yahoo.co.in

²Department of Mathematics, National Institute of Technology, Uttarakhand, Srinagar– 246174, **India**.

dtripathi@nituk.ac.in

³Department of Mechanical Engineering, Munzur University, Aktuluk street, Tunceli 62000, Tunceli, **Turkey**

nakkurt@munzur.edu.tr

⁴ Professor of Engineering Science and Director- Multi-Physical Engineering Sciences Group, Dept. Mechanical and Aeronautical Engineering, SEE, Salford University, Manchester, M54WT, **UK**. O.A.Beg@salford.ac.uk

***Corresponding author:** dtripathi@nituk.ac.in (D. Tripathi)

Abstract

Motivated by bio-inspired nano-technological functional coating flows, in the current paper a theoretical study of laminar, steady, incompressible bioconvection flow of a tangential hyperbolic (non-Newtonian) nanofluid from a bi-directional stretching surface under mutually orthogonal electrical and magnetic fields is presented. Nonlinear thermal radiation, Joule heating and heat source/sink effects are included. Non-Fourier and non-Fickian models are also implemented which feature thermal and solutal relaxation. Buongiorno's nanoscale model is adopted which features thermophoresis and Brownian motion effects. Rosseland's model is employed for thermal radiation. The electro-viscous effects arising from the distortions of the double-capacitance electric flow field are addressed with a modified formulation of the Poisson-Boltzmann equation. Via appropriate similarity transformations, the coupled, nonlinear partial differential conservation boundary layer equations and wall and freestream boundary conditions are rendered into a nonlinear ordinary differential boundary value problem which is solved numerically with an efficient numerical Lobatto - IIIa collocation method available in the MATLAB `bvp4c` shooting solver. Validation with previous studies is included. Velocity is strongly damped with increasing buoyancy ratio and bioconvection Rayleigh number are generally greater with positive rather than negative electrical field parameter. Increasing the Eckert number reduces the density of motile microorganisms while raising the temperature. An increment in Brownian motion and radiative parameters strongly accentuates temperatures.

Keywords: *Tangent hyperbolic nanofluid; magnetic field; electroosmosis; bioconvection; gyrotactic microorganisms; thermal radiation; Cattaneo-Christov double diffusion; functional coatings.*

NOMENCLATURE

- $(\bar{U}, \bar{V}, \bar{W})$ - velocity ($m s^{-1}$) in the direction of $(\bar{X}, \bar{Y}, \bar{Z})$ (m)
 β^* - thermal expansion coefficients ($1/K$)
 γ^* - average volume of a microorganism
 $\bar{\Phi}_{\bar{X}}$ - electric body force term ($V m^{-1}$)
 e – electron charge (C) ($kg^{1/2} m \Omega^{-1/2} sec^{-1/2}$)
 n_0 - ion density (m^{-3})
 ρ_e - net charge number density ($C m^{-3}$)
 ϵ_{eff} - electrical permittivity of the solution ($C V^{-1} m^{-1}$) ($m^{-1} \Omega^{-1} sec$)
 k_B - Boltzmann constant ($V m^{-1}$) ($kgm^2 sec^{-2} Kelvin^{-1}$)
 a, b – stretching rate (ms^{-1})
 c_p - specific heat at constant pressure ($J kg^{-1} K^{-1}$)
 τ - ratio of the effective heat capacitance of nanoparticles to base fluid
 \tilde{b} - chemotaxis constant for gyrotactic bioconvecting micro-organisms
 W_c - maximum cell swimming speed ($m s^{-1}$)
 \mathbf{V} - velocity vector ($m s^{-1}$)
 σ^* - electrical conductivity ($S m^{-1}$) ($\Omega^{-1} m^{-1}$)
 Q_0 - heat source (or sink) ($W m^{-3}$)
 B_0 - Uniform magnetic field ($kg^{1/2} m^{-1} sec^{-1/2} \Omega^{1/2}$)
 Γ - time-dependent material constant in tangent hyperbolic model
 g^* - gravitational acceleration ($m s^{-2}$)
 ρ_m - motile gyrotactic microorganism density ($kg m^{-3}$)
 ρ_p - nanoparticle density ($kg m^{-3}$)
 ρ_f - fluid density ($kg m^{-3}$)
 ν_f - kinematic viscosity ($m^2 sec^{-1}$)
 $\bar{\kappa}$ - thermal conductivity ($W m^{-1} K^{-1}$)
 α - thermal diffusivity ($m^2 s^{-1}$)
 D_B - Brownian diffusion ($m^2 s^{-1}$)
 D_T - thermophoresis diffusion coefficients ($m^2 s^{-1}$)
 D_m - microorganism diffusivity ($m^2 s^{-1}$)
 T_w -nanoparticle temperature at the wall (K)
 C_w -nanoparticle volume fraction (concentration) at the wall
 N_w -motile microorganism at the wall
 N_∞ -ambient value of motile microorganisms
 C_f -average concentration of nanoparticles
 C_∞ -ambient i. e. free stream value of nanoparticle volume fraction (concentration)
 T_∞ - ambient value of temperature (K)
 \bar{T} - dimensional temperature (K)
 \bar{C} - dimensional nanoparticle concentration
 \bar{N} - dimensional concentration (number density) of the microorganisms
 Γ_E -relaxation time of heat flux (non-Fourier thermal relaxation time)
 Γ_C -relaxation time of mass flux (non-Fickian solutal relaxation time)
 n -power law index parameter in tangent hyperbolic model
 We_1, We_2 - axial and transverse Weissenberg numbers

λ - mixed convection parameter
 Nr - buoyancy ratio parameter
 Nc - bioconvection Rayleigh number
 M - magnetic interaction number
 γ - axial to transverse stretching ratio (b/a)
 U_e - electric field parameter
 U_{HS} - Helmholtz-Smoluchowski velocity
 κ - electroosmosis parameter (inverse electrical double layer thickness)
 m - Debye-Hückel parameter
 Nb - Brownian parameter
 Nt - thermophoresis parameter
 Pr - Prandtl number
 Ec - Eckert number
 Rd - thermal radiation parameter
 Ω_T - thermal relaxation parameter
 Q - heat generation/absorption parameter
 Le - Lewis number
 Ω_C - concentration relaxation parameter
 Lb - bioconvection Lewis number
 Pe - Péclet number
 Ω - Microorganism density number difference variable
 ξ - zeta potential parameter.

1. INTRODUCTION

Functional materials are growing in popularity in the 21st century. These complex materials are responsive to external stimuli such as magnetic and electrical fields and provide more robust performance in a variety of applications including coatings [1-5]. The manufacture of such materials which also include smart nanomaterials frequently features *sheet stretching* processes. Such fabrication technologies rely heavily on boundary layer flows [6–8]. From an energy conservation standpoint, improving heat transfer in coating material synthesis [9, 10] is a critical factor and operations may also utilize very high temperatures where thermal radiation in addition to thermal convection and conduction modes arises. Heat transfer can be improved in many ways, such as changing the flow pattern, modifying the boundary conditions (via surface patterning) or increasing the thermal conductivity of the coating material. Many theoretical and experimental studies have shown that the thermal conductivity of micron-sized solid particles suspended in a base fluid leads to significant improvement in thermal efficiency. However, microparticles can generate agglomeration, abrasion and degradation in coatings. To circumvent these issues, smaller particles *engineered at the nanoscale* i. e. nanoparticles have been proposed. The resulting

colloidal mixture of nanoparticles and base fluids are termed *nanofluids*. Choi [11] first successfully engineered these colloidal suspension of submicron solid particles (nanoparticles) with a variety of base fluids and metallic and carbon-based nanoparticles and demonstrated significant elevation in thermal conductivity achieved by nanofluids as compared to conventional working fluids. In general, nanoparticles have a size of 1-50 nm. Since the nanoparticles are so small, nanofluids behave more like a single-phase fluid than a solid-liquid (two-phase) combination. Since nanoparticles are so small, nanofluids behave more like a single-phase liquid than a solid-liquid combination. In general, nanofluids are composed of chemically stable metals, carbides (SiC), oxides, nitrides (AlN, SiN), or non-metals (graphite, carbon nanotubes) with a conductive base fluid such as ethylene glycol (or other coolants), oil (or lubricants), biofluids, polymer solutions, water, etc. The thermal conductivity of nanofluids depends on the nanoparticle material, volume fraction, spatial distribution, particle size, shape, type of base fluid, temperature and pH. Metallic nanoparticles improve the electrical and thermal conductivity of the base fluid as well as the overall rate of heat transfer compared to non-metallic [12-13]. The heat transfer rate of nanofluids increases with the volume fraction of nanoparticles. Due to this unique ability, nanofluids can be used to dissipate heat from microsystems such as micro-heat pipes and microchannel heat sinks. Furthermore, they permit improved manipulation of heat transfer rates in coating extrusion manufacturing operations. According to Buongiorno [14], Brownian diffusion and thermophoresis dominate convective transport in nanofluids, necessitating their inclusion in the mass and energy conservation equations. Convective transport in nanofluids using the Buongiorno nanoscale model has been extensively studied for stretching sheet, stagnation and other boundary layer regimes of interest in materials processing and coating dynamics [15-18]. Electroosmosis is a fundamental electrokinetic phenomenon in which a peripheral electric field applied between the inlet and outlet drives the flow of an electrolyte or ionic fluid along a surface or between surfaces. In contrast, the neutral core is pushed and moved by the electric force like a solid [19]. In 1809, Reuss [20] confirmed this hypothesis using porous clay and initiated studies on electroosmotic fluid mechanics. This was followed by Helmholtz's 1879 theoretical study on electrical double layer (EDL) effects which provided a solid analytical foundation for electroosmotic transport [21]; in this work the properties of electrical current potential and fluids for electrokinetically driven motion were established. In the early 1900s, Smoluchowski [22] made significant progress in understanding electrokinetically driven flows, especially when the EDL

thickness is smaller than the channel height. Burgreen and Nakache [23] studied the effect of electrical surface potential on fluid flow through ultrafine slits using the linear Debye-Hueckel technique. More recently several investigators have considered electro-osmotic effects in coating flows. Melanson *et al.* [24] investigated experimentally the effects of buffer additives such as Mg^{2+} and hexamethonium to regulate electro-osmotic flow in dynamic capillary coatings via ion exchange onto the surface silanols. They also studied cationic polyelectrolytes or cationic surfactants which enable reversal of electro-osmotic flows. Bekri *et al.* [25] investigated the deployment of polyelectrolytes as successive multiple ionic coating polymers for protein separation in volatile background electrolyte systems, observing that separation efficiency and stability can be successfully manipulated in electroosmotic coating flows via this approach. Further studies of electro-osmotic coating flows include Qiao *et al.* [26] (on EDL effects), Hickey *et al.* [27] who deployed molecular dynamics simulation to compute cationic charge variation in electrokinetic polymer coatings, Li *et al.* [28] who examined the combined effects of nanoparticles and electroosmotic body force on internal surface nanochannel coatings. Additionally, Cao *et al.* [29] have employed dissipative particle dynamics computational methods to simulate charged polymer functional coatings under electro-osmotic effects. All these studies have confirmed that electroosmotic potential may be exploited to produce more stable and homogenous coatings for a variety of practical applications including stretchable electronics, biomedical devices and microfluidic designs.

Bioconvection is the movement of fluid due to a density gradient at the microscopic level, which is triggered by the self-propulsion of suspended motile organisms in the fluid. Bioconvection can be mobilized by different stimuli i. e. taxes including light, acidity, oxygen, magnetism, electrical field, chemical concentration etc. The taxes depend on the specific micro-organism under consideration. Bioconvection occurs via the collective behaviour of many micro-organisms swimming in the fluid and is observed as patterns [30-31]. *Gyrotaxis* is a common orientation mechanism observed in certain algae and bacteria and is generated from the balance of gravitational and viscous torques acting on bottom-heavy micro-organisms [32]. The continuum model for simulating bioconvection was introduced by Pedley and Kessler [33]. More recently doping coatings with micro-organisms has been explored by engineers as a bio-inspired design mechanism [34]. These new functional designs offer enhanced anti-bacterial properties and can be deployed in water-borne environments e. g. for marine engineering coating technologies, very

successfully. Several different bioconvection micro-organisms have also been explored in food safety [35] and bio-catalytic surface finishing for anti-microbial designs [36]. Mathematical models of bioconvection boundary layer flows have also been developed in recent years. Aneja *et al.* [37] used a finite element variational method to compute the effects of non-uniform magnetic field on hydromagnetic bioconvection boundary layer flow along an inclined stretching plane. Nima *et al.* [38] used finite difference methods to simulate the free/forced bioconvection flow with gyrotactic microorganisms along a fuel cell wall adjacent to a Darcian porous medium. Quite recently bioconvection in different micro-organisms has been combined with different nanoparticles (e. g. gold, silver) to achieve dual benefits in coating technologies [39, 40, 41]. Kuznetsov [42-44] was the first to study bioconvection in nanofluids, assuming that the micro-organisms and nanoparticles do not interact and that the nanofluid is a dilute suspension. Boundary layer coating models of bioconvection nanofluid transport were developed for slip effects and stretching/shrinking walls by Bég *et al.* [45]. Bég [46] examined the spin coating in Von Karman swirling gyrotactic bioconvection nanofluid flow from a rotating disc using numerical methods. Further studies include Qin [47] on nanomaterial irreversibility and convective transportation; Abdelkader *et al.* [48] on Al₂O₃-water-based nanofluid and cooling the glass cover and Sen [49] on Green nanofiber mat from HLM–PVA–Pectin using an electrospinning technique.

The above studies were generally confined to *Newtonian* nanofluid bioconvection. Many smart coating materials however exhibit non-Newtonian characteristics. These include shear-thinning, shear-thickening, viscoelasticity, stress relaxation and retardation. Robust rheological models are required to accurately simulate functional bio-nano-coatings. A number of such studies have therefore been communicated also including a spectrum of other multi-physical effects. In this context nanofluid bioconvection rheological flows have been addressed by Waqas *et al.* [50] who implemented the Reiner-Rivlin second order viscoelastic model). Khan *et al.* [51] deployed the Stokes polar couple stress model and also considered magnetic field and wall slip effects. Zaman *et al.* [52] applied the Williamson non-Newtonian model and furthermore included thermal radiative flux and hydromagnetic (Lorentz) body force effects. An alternative rheological model is the tangent hyperbolic model which can accurately predict shear thinning phenomena in non-Newtonian nanofluids and also viscoelastic effects. This model has been utilized in several nanofluid coating flow studies. Bahsa *et al.* [53] used a Keller box finite difference code and the second law of thermodynamics to analyze the entropy production in tangent hyperbolic nanofluid

coating boundary layer flow external to a cylindrical body. Wang *et al.* [54] investigated microorganism doping in a tangential hyperbolic nanofluid flow with Wu slip and wall transpiration, noting that motile micro-organism density decreases with Péclet number. Kumaran *et al.* [55] used finite element and finite difference methods to compute the magneto-gyrotactic bioconvection tangent hyperbolic reactive nanofluid coating flow on a cylinder in porous media. They showed that increasing the power law index accelerates the flow whereas elevation in Weissenberg number boosts the heat transfer boundary layer thickness of tangent hyperbolic nanofluid. They also found that there is a depletion in microorganism density number with larger values of bioconvection Schmidt number and Peclet number. Further studies include Shafiq *et al.* [56] who examined the tangential hyperbolic magnetic nanofluid flow with gyrotactic microorganisms from an exponentially stretching surface.

In many coating flows, the surface may be stretched in one dominant direction or two directions [57]. The latter is known as *bi-directional stretching* and permits enhanced control of material constitution during fabrication. Wang [58] was among the first researchers to analyze the bi-directional stretching of a Newtonian coating sheet, for which he derived exact similarity solutions of the Navier–Stokes equations. More recently Shahid *et al.* [59] have used a Chebychev spectral collocation method to compute the magnetic functional polymer flow from a bi-directional stretching parabolic surface in permeable media. Amirsom *et al.* [60] have used MAPLE quadrature to simulate the bioconvection nanofluid boundary layer flow from a bi-axial stretching sheet with multiple wall slip effects. These studies have shown that different stretching rates in orthogonal directions substantially influence heat, mass and momentum characteristics.

In view of these studies, bioconvection in nanofluids achieves superior thermal performance compared with bioconvection in ordinary fluids. Engineering systems such as smart coatings can be better controlled and manipulated if electrical and magnetic fields are combined. According to a review of the scientific literature, the combined electroosmotic and magnetohydrodynamic (MHD) radiative nanofluid bioconvection (gyrotactic microorganism) flow from a bi-directional stretching surface has not yet been investigated. This is the focus of the present study which as elaborated earlier is motivated by studying emerging complex functional material manufacturing processes including electromagnetic hydrogels [61] and bio-nano-coatings [62]. To achieve more realistic results both non-Fourier thermal relaxation and non-Fickian solutal relaxation effects are included i. e. the *Cattaneo-Christov laws* are used to study the heat and mass transport.

Buongiorno's nanoscale model is deployed which permits the inclusion of nanoparticle species diffusion. Furthermore, thermal radiative heat flux, viscous heating, Joule heating and heat source/sink effects are incorporated in the model developed. Rosseland's model is employed for thermal radiation. The electro-viscous effects arising from the distortions of the double-capacitance electric flow field are addressed with a modified formulation of the Poisson-Boltzmann equation. The transformed, dimensionless, self-similar ordinary differential conservation boundary layer equations with associated wall and freestream boundary conditions are solved numerically with an efficient Lobatto - IIIa collocation method available in the MATLAB bvp4c shooting solver. Validation with previous studies is included. Extensive visualization of the effects of emerging parameters on velocity, temperature, nanoparticle concentration and motile micro-organism density is included. Tables for local Sherwood number (nanoparticle mass transfer rate) and local microorganism density number gradient are also provided.

2. BI-DIRECTIONAL STRETCHING NANO-BIO COATING FLOW MODEL

2.1 Flow modeling

Consider the steady, incompressible, viscous, 3-dimensional bioconvective electromagnetic tangent hyperbolic nanofluid flow containing motile gyrotactic microorganisms on a bi-directional stretching surface as shown in **Fig.1**. Nonlinear thermal radiation, Joule heating and heat sink/source effects are included. Hall current effects are ignored. The nanofluid is magnetic, ionic and also optically thick. A Cartesian coordinate system $(\bar{X}, \bar{Y}, \bar{Z})$ is adopted. The stretching motion is in the $\bar{X} - \bar{Y}$ plane and the \bar{Z} axis is normal to this plane. The surface stretching velocities in the \bar{X}, \bar{Y} directions are $U_w(\bar{X}) = a\bar{X}, V_w(\bar{Y}) = b\bar{Y}$, respectively.

2.2 Governing equations

For three-dimensional flow of an electromagnetic hyperbolic tangential nanofluid with microorganisms the boundary layer equations are developed below.

2.2.1 Continuity and momentum equations

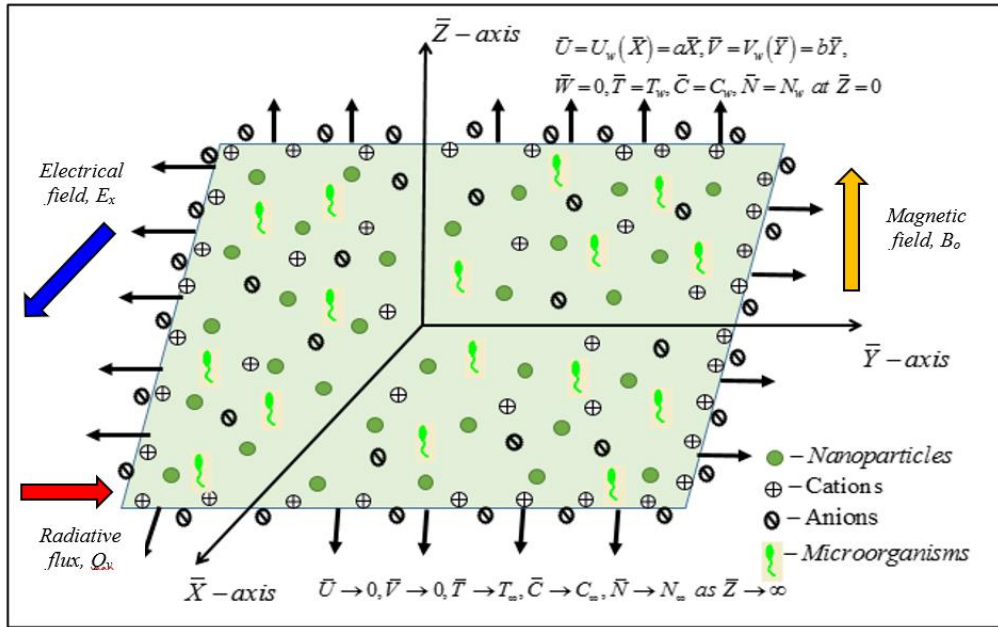


Fig. 1: Physical model for 3-dimensional bioconvective electromagnetic hyperbolic tangent nanofluid flow on a bi-directional stretching surface

A transverse magnetic field acts normal to the stretching plane. The bi-directional stretching induces both a primary flow and a secondary flow and the regime is therefore 3-dimensional in nature. The tangent hyperbolic rheological model introduces a power law index and modified shear terms. The relevant conservation *i. e.* mass and momenta equations for tangent hyperbolic non-Newtonian fluid following Wang *et al.* [54] can be written with magnetic and electrical body forces as:

$$\frac{\partial \bar{U}}{\partial \bar{X}} + \frac{\partial \bar{V}}{\partial \bar{Y}} + \frac{\partial \bar{W}}{\partial \bar{Z}} = 0, \quad (1)$$

$$\bar{U} \frac{\partial \bar{U}}{\partial \bar{X}} + \bar{V} \frac{\partial \bar{U}}{\partial \bar{Y}} + \bar{W} \frac{\partial \bar{U}}{\partial \bar{Z}} = \nu_f (n-1) \frac{\partial^2 \bar{U}}{\partial \bar{Z}^2} + \nu_f n \sqrt{2} \Gamma \frac{\partial \bar{U}}{\partial \bar{Z}} \left(\frac{\partial^2 \bar{U}}{\partial \bar{Z}^2} \right) + \bar{\rho}_e \bar{\Phi}_{\bar{X}} - \frac{\sigma^* B_0^2}{\rho_f} \bar{U} + \bar{F}, \quad (2)$$

$$\bar{U} \frac{\partial \bar{V}}{\partial \bar{X}} + \bar{V} \frac{\partial \bar{V}}{\partial \bar{Y}} + \bar{W} \frac{\partial \bar{V}}{\partial \bar{Z}} = \nu_f (n-1) \frac{\partial^2 \bar{V}}{\partial \bar{Z}^2} + \nu_f n \sqrt{2} \Gamma \frac{\partial \bar{V}}{\partial \bar{Z}} \left(\frac{\partial^2 \bar{V}}{\partial \bar{Z}^2} \right) - \frac{\sigma^* B_0^2}{\rho_f} \bar{V}, \quad (3)$$

Where $\bar{F} = (1 - C_f) \beta^* g^* (\bar{T} - T_\infty) - \frac{(\rho_p - \rho_f) g^* (\bar{C} - C_\infty)}{\rho_f} - \frac{(\rho_m - \rho_f) g^* \gamma^* (\bar{N} - N_\infty)}{\rho_f}$, is an effective body

force with thermal, nanoparticle concentration and micro-organism buoyancy force contributions.

2.2.2 Energy equation

Heat flux(\bar{q}) fulfills the subsequent expressions in terms of Cattaneo – Christov theory [55]:

$$\bar{q} + \Gamma_E \left[\frac{\partial \bar{q}}{\partial \bar{t}} + \mathbf{V} \cdot \nabla \bar{q} + (\nabla \cdot \mathbf{V}) \bar{q} - \bar{q} \nabla \cdot \mathbf{V} \right] = -\bar{\kappa} \nabla \cdot \bar{T}, \quad (4)$$

The Fourier's theory of heat flux can be retrieved by setting thermal relaxation parameter, $\Gamma_T = 0$ and becomes *parabolic* rather than the non-Fourier theory which is *hyperbolic*. For an incompressible liquid, the above non-Fourier expression has the form:

$$\bar{q} + \Gamma_E \left[\frac{\partial \bar{q}}{\partial \bar{t}} + \mathbf{V} \cdot \nabla \bar{q} \right] = -\bar{\kappa} \nabla \cdot \bar{T}, \quad (5)$$

The energy conservation law can be written as:

$$(\rho c)_p \mathbf{V} \cdot \nabla \bar{T} = \nabla \cdot \bar{q}, \quad (6)$$

Now eliminating \bar{q} from Eqns. (5) and (6), yields the energy equation in steady state form as follows:

$$\begin{aligned} \bar{U} \frac{\partial \bar{T}}{\partial \bar{X}} + \bar{V} \frac{\partial \bar{T}}{\partial \bar{Y}} + \bar{W} \frac{\partial \bar{T}}{\partial \bar{Z}} + \Gamma_E \lambda_E = & \left(\alpha + \frac{1}{\rho_f c_p} \frac{16 \bar{\sigma} T_\infty^3}{3 \bar{k}} \right) \frac{\partial^2 \bar{T}}{\partial \bar{Z}^2} + \tau \left\{ D_B \frac{\partial \bar{C}}{\partial \bar{Z}} \frac{\partial \bar{T}}{\partial \bar{Z}} + \frac{D_T}{T_\infty} \left(\frac{\partial \bar{T}}{\partial \bar{Z}} \right)^2 \right\} \\ & + \frac{\sigma^* B_0^2}{\rho_f c_p} u^2 + \frac{Q_0 (\bar{T} - T_\infty)}{\rho_f c_p} + \frac{v_f}{c_p} (1 - n) \left(\frac{\partial \bar{U}}{\partial \bar{Z}} \right)^2, \end{aligned} \quad (7)$$

where $\lambda_E = \left(\bar{U} \frac{\partial}{\partial \bar{X}} + \bar{V} \frac{\partial}{\partial \bar{Y}} + \bar{W} \frac{\partial}{\partial \bar{Z}} \right) \left(\bar{U} \frac{\partial \bar{T}}{\partial \bar{X}} + \bar{V} \frac{\partial \bar{T}}{\partial \bar{Y}} + \bar{W} \frac{\partial \bar{T}}{\partial \bar{Z}} \right)$.

2.2.3 Nanoparticle concentration equation

The nanoparticle mass flux(\bar{J}) in term of Cattaneo-Christov theory [63] is defined as follows:

$$\bar{J} + \Gamma_C \left[\frac{\partial \bar{J}}{\partial \bar{t}} + \mathbf{V} \cdot \nabla \bar{J} + (\nabla \cdot \mathbf{V}) \bar{J} - \bar{J} \nabla \cdot \mathbf{V} \right] = -D_B \nabla \cdot \bar{C}, \quad (8)$$

The classical Fick's law can be obtained by substituting $\Gamma_C = 0$ in Eqn. (8). The above expression can be written as:

$$\bar{J} + \Gamma_C \left[\frac{\partial \bar{J}}{\partial \bar{t}} + \mathbf{V} \cdot \nabla \bar{J} \right] = -D_B \nabla \cdot \bar{C}, \quad (9)$$

The nanoparticle concentration equation in steady state form may be stated as:

$$\mathbf{V} \cdot \nabla \bar{C} = \nabla \cdot \bar{J}, \quad (10)$$

Now eliminating \bar{J} from Eqns. (9) and (10), produces the nanoparticle concentration equation as follows:

$$\bar{U} \frac{\partial \bar{C}}{\partial \bar{X}} + \bar{V} \frac{\partial \bar{C}}{\partial \bar{Y}} + \bar{W} \frac{\partial \bar{C}}{\partial \bar{Z}} + \Gamma_C \lambda_C = D_B \frac{\partial^2 \bar{C}}{\partial \bar{Z}^2} + \frac{D_T}{T_\infty} \left(\frac{\partial^2 \bar{T}}{\partial \bar{Z}^2} \right), \quad (11)$$

where $\lambda_c = \left(\bar{U} \frac{\partial}{\partial \bar{X}} + \bar{V} \frac{\partial}{\partial \bar{Y}} + \bar{W} \frac{\partial}{\partial \bar{Z}} \right) \left(\bar{U} \frac{\partial \bar{C}}{\partial \bar{X}} + \bar{V} \frac{\partial \bar{C}}{\partial \bar{Y}} + \bar{W} \frac{\partial \bar{C}}{\partial \bar{Z}} \right)$.

2.2.4 Equation for motile micro-organisms transport (self-propulsion)

Gyrotactic microorganism density number may be represented as follows:

$$\nabla \cdot \bar{M} = 0, \quad (12)$$

\bar{M} flux can be extended according to Kuznetsov [42] as:

$$\bar{M} = \bar{N} \vec{V} + \bar{N} \vec{\nabla} - D_n \nabla \bar{N}, \quad (13)$$

Here $\vec{V} = \left(\frac{W_C b}{C_w - C_\infty} \right) \nabla \bar{C}$, micro-organism diffusivity is symbolized by D_n , W_C is the maximum velocity of a cell movement and the chemotaxis constant is b (Note- the product $W_C b$ is viewed as constant). Effectively the conservation equation for number density of gyrotactic micro-organisms can be written as [66-67]:

$$\bar{U} \frac{\partial \bar{N}}{\partial \bar{X}} + \bar{V} \frac{\partial \bar{N}}{\partial \bar{Y}} + \bar{W} \frac{\partial \bar{N}}{\partial \bar{Z}} + \frac{b W_C}{C_w - C_\infty} \left(\frac{\partial}{\partial \bar{X}} \left(\bar{N} \frac{\partial \bar{C}}{\partial \bar{X}} \right) + \frac{\partial}{\partial \bar{Y}} \left(\bar{N} \frac{\partial \bar{C}}{\partial \bar{Y}} \right) + \frac{\partial}{\partial \bar{Z}} \left(\bar{N} \frac{\partial \bar{C}}{\partial \bar{Z}} \right) \right) = D_m \left(\frac{\partial^2 \bar{N}}{\partial \bar{X}^2} + \frac{\partial^2 \bar{N}}{\partial \bar{Y}^2} + \frac{\partial^2 \bar{N}}{\partial \bar{Z}^2} \right). \quad (14)$$

2.2.5 Boundary conditions for the regime

The wall and free stream boundary conditions prescribed for solving Eqns. (1)-(3), (7), (11) and (14) are expressed as:

$$\left. \begin{aligned} \bar{U} = U_w(\bar{X}) = a\bar{X}, \bar{V} = V_w(\bar{Y}) = b\bar{Y}, \bar{W} = 0, \bar{T} = T_w, \bar{C} = C_w, \bar{N} = N_w \text{ at } \bar{Z} = 0, \\ \bar{U} \rightarrow 0, \bar{V} \rightarrow 0, \bar{T} \rightarrow T_\infty, \bar{C} \rightarrow C_\infty, \bar{N} \rightarrow N_\infty \text{ as } \bar{Z} \rightarrow \infty. \end{aligned} \right\} \quad (15)$$

2.3. Analysis of electroosmosis

The coating material considered in Fig. 1 is an ionic nanofluid. This possesses an electrostatic potential due to the formation of an electric double layer (EDL) which is defined by the Poisson equation [24-27, 37]:

$$\nabla^2 \bar{\Phi} = - \frac{\bar{\rho}_e}{\varepsilon_{eff}}, \quad (16)$$

Here $\varepsilon_{eff} = \varepsilon_0 \varepsilon_r$ in which vacuum permittivity is specified by ε_0 and ε_r refers to dielectric constant of the medium (nanofluid coating). Assuming that cations and anions have the same valence \bar{z} , the charge number density for symmetric electrolyte solutions (ionic nanofluids) is calculated as:

$$\bar{\rho}_e = e\bar{z}(n^+ - n^-), \quad (17)$$

Here n^+ and n^- are the number of cations and anions, with the electronic charge e and n_0 is the mass concentration of ions. Based on this assumption, a linearized Poisson-Boltzmann distribution can be used to accurately describe the electrical potentials inside the nanofluid coating boundary layer regime with an electrical double layer (EDL) smaller than half the thickness of the surface plate. The Boltzmann ion number concentration is defined as follows:

$$n^\pm = e^{\mp \frac{e\bar{z}\bar{\Phi}}{k_B T_v}}, \quad (18)$$

Substituting Eqn. (18) into Eqn. (17), we obtain:

$$\bar{\rho}_e = -2\bar{z}en_0 \sinh\left(\frac{\bar{z}e\bar{\Phi}}{k_B T_v}\right), \quad (19)$$

Substituting the value of charge density (Eqn. (19)) into Poisson's equation (Eqn. (16)), the following differential equation for electrical potential emerges:

$$\frac{\partial^2 \bar{\Phi}}{\partial \bar{x}^2} + \frac{\partial^2 \bar{\Phi}}{\partial \bar{y}^2} + \frac{\partial^2 \bar{\Phi}}{\partial \bar{z}^2} = \frac{2\bar{z}en_0}{\epsilon_{eff}} \sinh\left(\frac{\bar{z}e\bar{\Phi}}{k_B T_v}\right), \quad (20)$$

The following boundary condition for the electric potential is assumed:

$$\bar{\Phi} = \bar{\xi} \text{ at } \bar{Z} = 0 \text{ and } \bar{\Phi} \rightarrow 0 \text{ as } \bar{Z} \rightarrow \infty. \quad (21)$$

2.4 Dimensionless variables and reduction of governing equations

In order to reduce the governing system of partial differential equations to nonlinear non-dimensional ordinary differential equations, the following dimensionless variables are invoked:

$$\bar{U} = a\bar{X}f'(\eta), \bar{V} = b\bar{Y}g'(\eta), \bar{W} = -\sqrt{av_f} [f(\eta) + g(\eta)],$$

$$\theta(\eta) = \frac{\bar{T} - T_\infty}{T_w - T_\infty}, \varphi(\eta) = \frac{C - C_\infty}{C_w - C_\infty}, \chi(\eta) = \frac{N - N_\infty}{N_w - N_\infty}, \Phi = \frac{\bar{z}e\bar{\Phi}}{k_B T_v}, \eta = \bar{Z} \sqrt{\frac{a}{v_f}}. \quad (22)$$

Eqn. (1) is automatically satisfied by applying the correct similarity transformation (22), and Eqns. (2)-(3), (7), (11), (14) and (20) which comprise the full model, become the following ordinary differential conservation equations for *primary momentum (axial)*, *secondary momentum (transverse)*, *energy*, *nanoparticle concentration*, *micro-organism number density* and *electrical potential*:

$$\left(nWe_1 f'' + (1-n)\right) f''' - f'^2 + (f+g)f'' + \lambda(\theta - Nr\varphi - Nc\chi) - Mf' + U_e \Phi'' = 0, \quad (23)$$

$$g''(f+g) - g'^2 + g'''[nWe_2 g'' + (1-n)] - Mg' = 0, \quad (24)$$

$$(1 + Rd)\theta'' + Pr \theta' (f + g) + Pr Nb \theta' \varphi' + Pr Nt(\theta')^2 + M Pr Ec f'^2 + Pr Q \theta + (1 - n)Ec f'^2 - Pr \Omega_T \left((f' + g')\theta'(f + g) + (f + g)^2 \theta'' \right) = 0, \quad (25)$$

$$\varphi'' + Le Pr (f + g) \varphi' + \frac{Nt}{Nb} \theta'' - Le Pr \Omega_C \left((f' + g')(f + g)\varphi' + (f + g)^2 \varphi'' \right) = 0, \quad (26)$$

$$\chi'' + Lb(f + g)\chi' - Pe(\chi' \varphi' + (\Omega + \chi)\varphi'') = 0, \quad (27)$$

$$\Phi'' - \kappa^2 \sinh(\Phi) = 0. \quad (28)$$

The complete set of dimensionless boundary conditions can be expressed as follows:

$$\left. \begin{aligned} f' = 1, g' = \gamma, f = 0, g = 0, \theta = 1, \varphi = 1, \chi = 1, \Phi = \xi at \eta = 0 \\ f' \rightarrow 0, g' \rightarrow 0, \theta \rightarrow 0, \varphi \rightarrow 0, \chi \rightarrow 0, \Phi \rightarrow 0 \text{ as } \eta \rightarrow \infty. \end{aligned} \right\} \quad (29)$$

In Eqns. (23)-(29), the following non-dimensional parameters arise: Primary and secondary

Weissenberg numbers associated with the bi-directional stretching, $We_1 = \sqrt{\frac{2a}{v_f}} a \bar{X} \Gamma$, $We_2 =$

$\sqrt{\frac{2a}{v_f}} a \bar{Y} \Gamma$, mixed convection parameter $\lambda = \frac{(1 - C_f) \beta^* g^* (T_w - T_\infty)}{a U_w}$, buoyancy ratio parameter $Nr =$

$\frac{(\rho_p - \rho_f)(C_w - C_\infty)}{\rho_f(1 - C_\infty)(T_w - T_\infty)\beta^*}$, bioconvection Rayleigh number $Nc = \frac{\gamma^*(\rho_m - \rho_f)(N_w - N_\infty)}{\rho_f(1 - C_\infty)(T_w - T_\infty)\beta^*}$ magnetic interaction

number $M = \frac{\sigma^* B_0^2}{a \rho_f}$, stretching rate ratio $\gamma = \frac{b}{a}$, which is based on the ratio of the stretching rate

velocities i.e. $\bar{U} = a \bar{X} f'(\eta)$, $\bar{V} = b \bar{Y} g'(\eta)$, electric field parameter $U_e = \frac{1}{a U_w} U_{HS}$ in which $U_{HS} =$

$-\frac{k_B T_v \epsilon_{eff} \bar{\Phi} \bar{X}}{\mu_f \bar{z} e}$ is the Helmholtz-Smoluchowski velocity, electroosmosis parameter $\kappa^2 = m^2 \frac{v_f}{a}$ in

which $m^2 = -\frac{2 \bar{z}^2 e^2 n_0}{\epsilon_{eff} k_B T_v}$ is the Debye-Hückel parameter, Brownian dynamics parameter $Nb =$

$\frac{\tau D_B (C_w - C_\infty)}{v_f}$, thermophoresis parameter $Nt = \frac{\tau D_T (T_w - T_\infty)}{T_\infty v_f}$, Prandtl number $Pr = \frac{v_f}{\alpha}$, Eckert number

$Ec = \frac{U_w^2}{c_p (T_w - T_\infty)}$, thermal radiation parameter $Rd = \frac{16 \sigma T_\infty^3}{3 k \bar{\kappa}}$, thermal relaxation $\Omega_T = a \Gamma_E$, heat

generation/absorption $Q = \frac{Q_0}{a \rho c_p}$, Lewis number $Le = \frac{\alpha}{D_B}$, concentration (mass) relaxation $\Omega_C =$

$a \Gamma_C$, bioconvection Lewis number $Lb = \frac{v_f}{D_m}$, Péclet number $Pe = \frac{\bar{b} W_C}{D_m}$, microorganisms difference

variable $\Omega = \frac{N_\infty}{N_w - N_\infty}$ and zeta potential parameter $\xi = \frac{\bar{z} e \bar{\xi}}{k_B \bar{T}_H}$. Furthermore, it is useful to define

physical quantities for characterising the nanoparticle mass transfer and micro-organism transfer rates at the wall. These are the local Sherwood and motility density numbers are defined as follows:

$$Sh_x = \frac{q_C \bar{X}}{(C_w - C_\infty) D_B}, Sn_x = \frac{q_N \bar{X}}{(N_w - N_\infty) D_m}. \quad (30)$$

Here the nanoparticle and micro-organism mass fluxes are:

$$q_C = -D_B \left(\frac{\partial \bar{C}}{\partial \bar{Z}} \right)_{\bar{Z}=0}, q_N = -D_m \left(\frac{\partial \bar{N}}{\partial \bar{Z}} \right)_{\bar{Z}=0}.$$

In non-dimensional form the relevant expressions for local Sherwood number and micro-organism density number gradient are:

$$\frac{Sh_x}{\sqrt{Re_x}} = -\varphi'(0); \frac{Sn_x}{\sqrt{Re_x}} = -\chi'(0). \quad (31)$$

Here local Reynolds number $Re_x = \frac{\bar{X} U_w}{\nu_f}$ is used based on the primary stretching direction.

3. NUMERICAL SOLUTION WITH MATLAB SOFTWARE AND VALIDATION

The nonlinearity of the coupled ordinary differential Eqns. (23)-(28) with associated boundary conditions (29), renders analytical solutions impractical. Therefore, computational solutions are sought using the MATLAB's bvp4c shooting technique. This utilizes a Lobatto - IIIa collocation method. Using appropriate variables, the higher order differential equations are reduced to first order equations, as follows:

$$f = y_1; f' = y_2; f'' = y_3; f''' = y_3'; g = y_4; g' = y_5; g'' = y_6; g''' = y_6'; \theta = y_7; \theta' = y_8; \theta'' = y_8'; \varphi = y_9; \varphi' = y_{10}; \varphi'' = y_{10}'; \chi = y_{11}; \chi' = y_{12}; \chi'' = y_{12}'; \Phi = y_{13}; \Phi' = y_{14}; \Phi'' = y_{14}'. \quad (32)$$

Here the following definitions apply:

$$y_3' = \frac{1}{nWe_1 y_3^{-n+1}} (y_2^2 - (y_1 + y_4) y_3 - \lambda(y_7 - Nry_9 - Ncy_{11}) + My_2 - Uek^2 \sinh(y_{13})), \quad (33)$$

$$y_5' = \frac{1}{nWe_2 y_6^{-n+1}} (y_5^2 - (y_1 + y_4) y_6 + My_5), \quad (34)$$

$$y_8' =$$

$$\frac{1}{(1+Rd-Pr\Omega_T(y_1+y_4)^2)} \left(Pr\Omega_T y_8 (y_1 + y_4)(y_2 + y_5) - (1-n)Ecy_3^2 - Pr y_8 (y_1 + y_4) \right), \quad (35)$$

$$y_{10}' = \frac{1}{(1+LePr\Omega_C(y_1+y_4)^2)} \left(LePr\Omega_C y_{10} (y_1 + y_4)(y_2 + y_5) - LePr y_{10} (y_1 + y_4) - \frac{Nt}{Nb} y_8' \right), \quad (36)$$

$$y_{12}' = Pe(y_{12} y_{10} + y_{10}' (\Omega + y_{11})) - Lby_{12} (y_1 + y_4), y_{14}' = \kappa^2 \sinh(y_{13}). \quad (37)$$

The boundary conditions are prescribed in MATLAB bvp4c as follows:

$$\left. \begin{aligned} y_2 = 1, y_5 = \gamma, y_1 = 0, y_4 = 0, y_7 = 1, y_9 = 1, y_{11} = 1, y_{13} = \xi at\eta = 0 \\ y_2 \rightarrow 0, y_5 \rightarrow 0, y_7 \rightarrow 0, y_9 \rightarrow 0, y_{11} \rightarrow 0, y_{13} \rightarrow 0 \text{ as } \eta \rightarrow \infty. \end{aligned} \right\} \quad (34)$$

To validate the numerical solutions described in the next section, benchmarking with previous simpler studies from the literature is conducted. **Table 1** shows the primary (axial) and secondary (transverse) skin friction i. e. velocity gradients at the wall compared with Wang [55] and Hayat *et al.* [64]. Excellent correlation is obtained for a range of stretching ratio parameter values ($\gamma = \frac{b}{a}$) for the case where *electrical, magnetic, nanofluid and bioconvection* effects are negated. Confidence in the present MATLAB solutions is therefore confirmed.

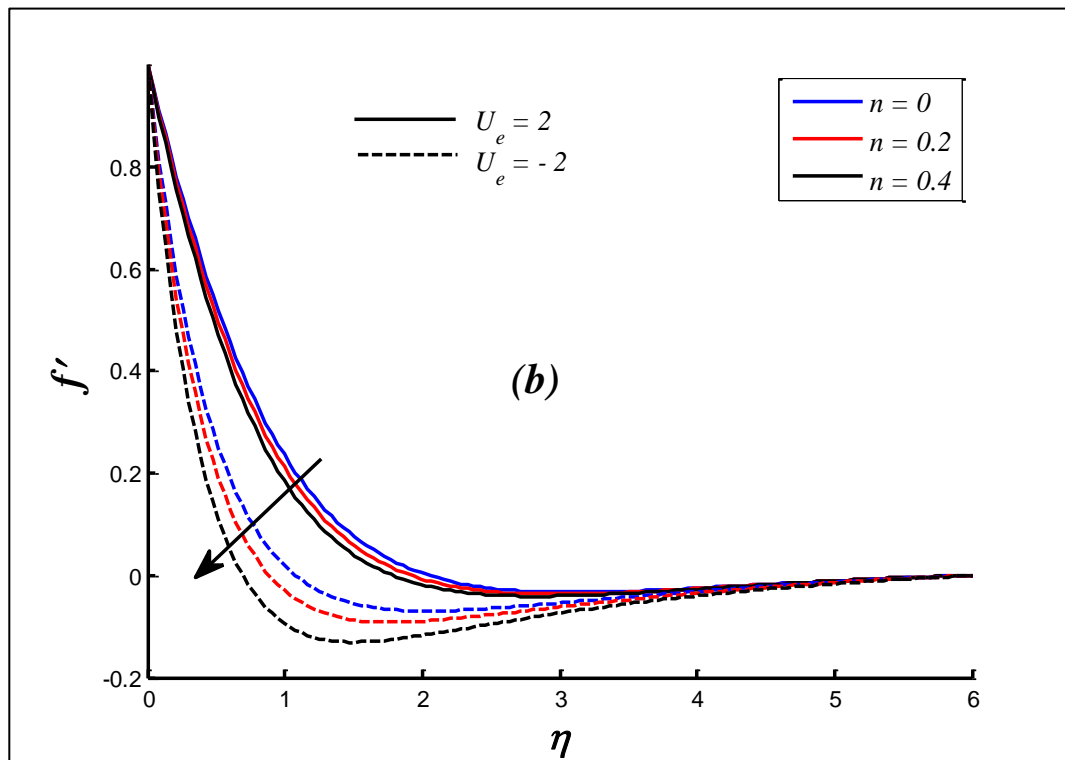
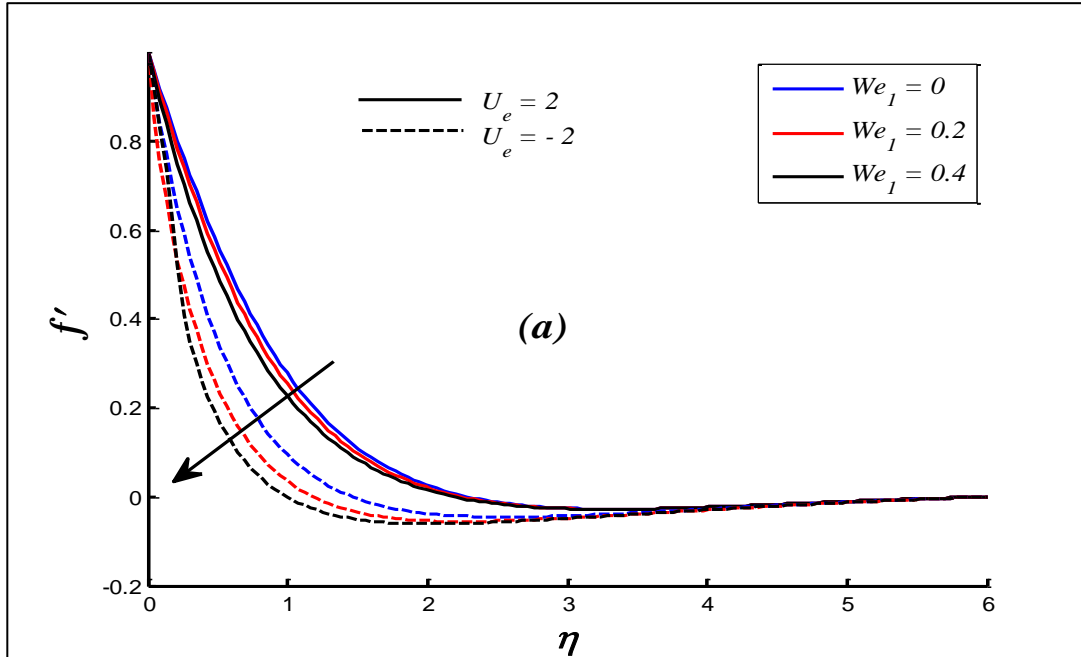
Table 1: Comparative data for different values of γ with Wang [55] and Hayat *et al.* [64] for the absence of the $\lambda = M = U_e = 0$ and $n = 0$.

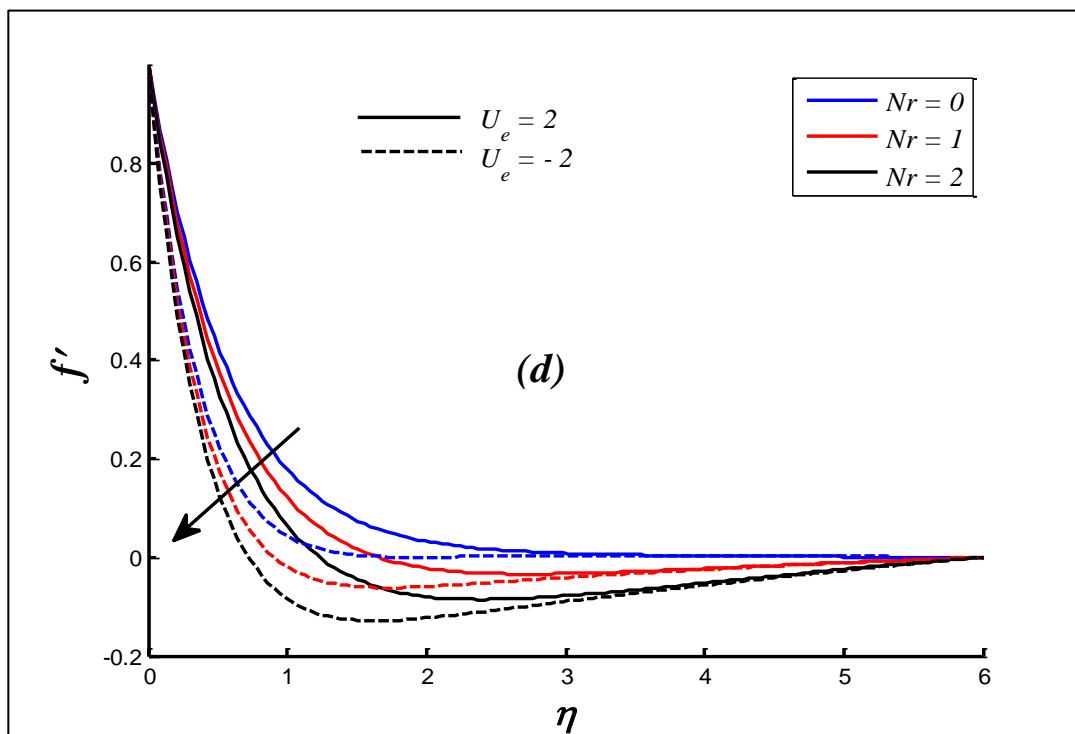
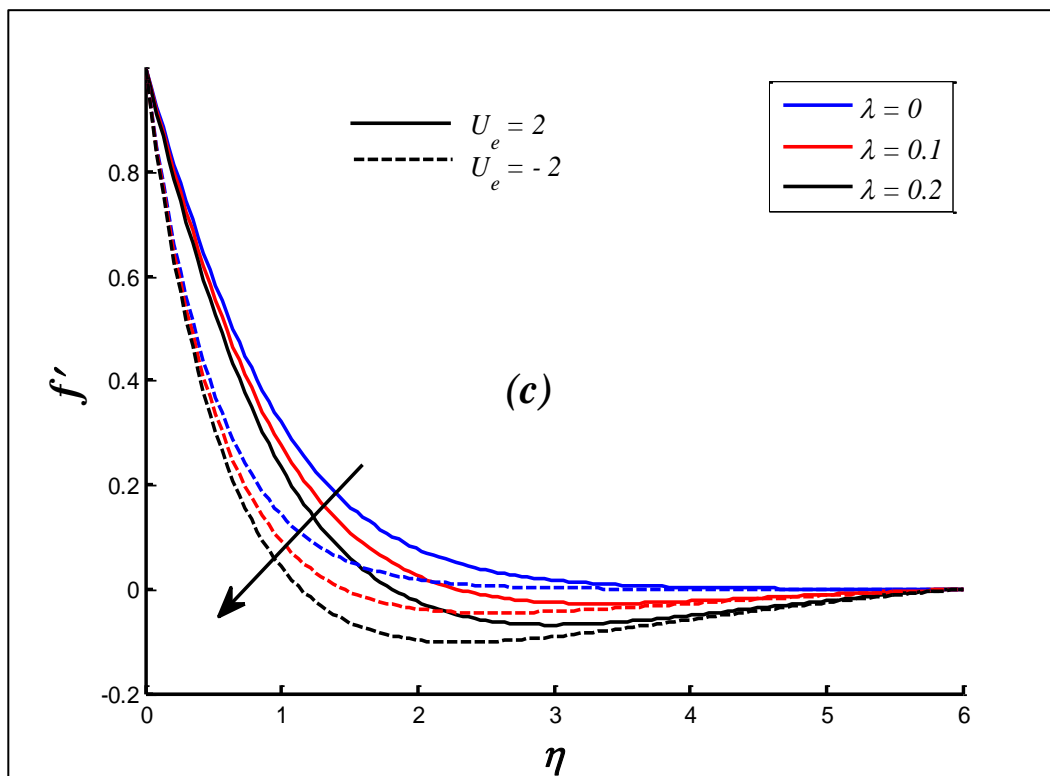
γ	Present MATLAB bvp4c results		Wang [55]		Hayat <i>et al.</i> [64].	
	$-f''(0)$	$-g''(0)$	$-f''(0)$	$-g''(0)$	$-f''(0)$	$-g''(0)$
0	1.000062482423727	0	1	0	1.0	0
0.10	1.020300418083956	0.066859434360486	--	--	1.020260	0.668472
0.20	1.039522965336466	0.148750458516618	--	--	1.039495	0.148737
0.25	1.048834372997002	0.194576788554375	1.048813	0.194564	1.048810	0.19457
0.30	1.057974439764333	0.243371878755454	--	--	1.057955	0.243360
0.40	1.075802327844086	0.349218734209357	--	--	1.075880	0.349209
0.5	1.093105441666520	0.465213017843099	1.093097	0.465205	1.093095	0.465205
0.6	1.109954659937748	0.590535464860613	--	--	1.109942	0.590529
0.7	1.126403245925845	0.724536912744527	--	--	1.126398	0.724532
0.75	1.134490705802878	0.794622858170999	1.134485	0.794622	1.134500	0.794620
0.8	1.142492898714836	0.866686975477697	--	--	1.142489	0.866683
0.9	1.158257049643253	1.016541855969542	--	--	1.158254	1.016539
1	1.173723095061049	1.173723095061331	1.173720	1.173720	1.173721	1.173721

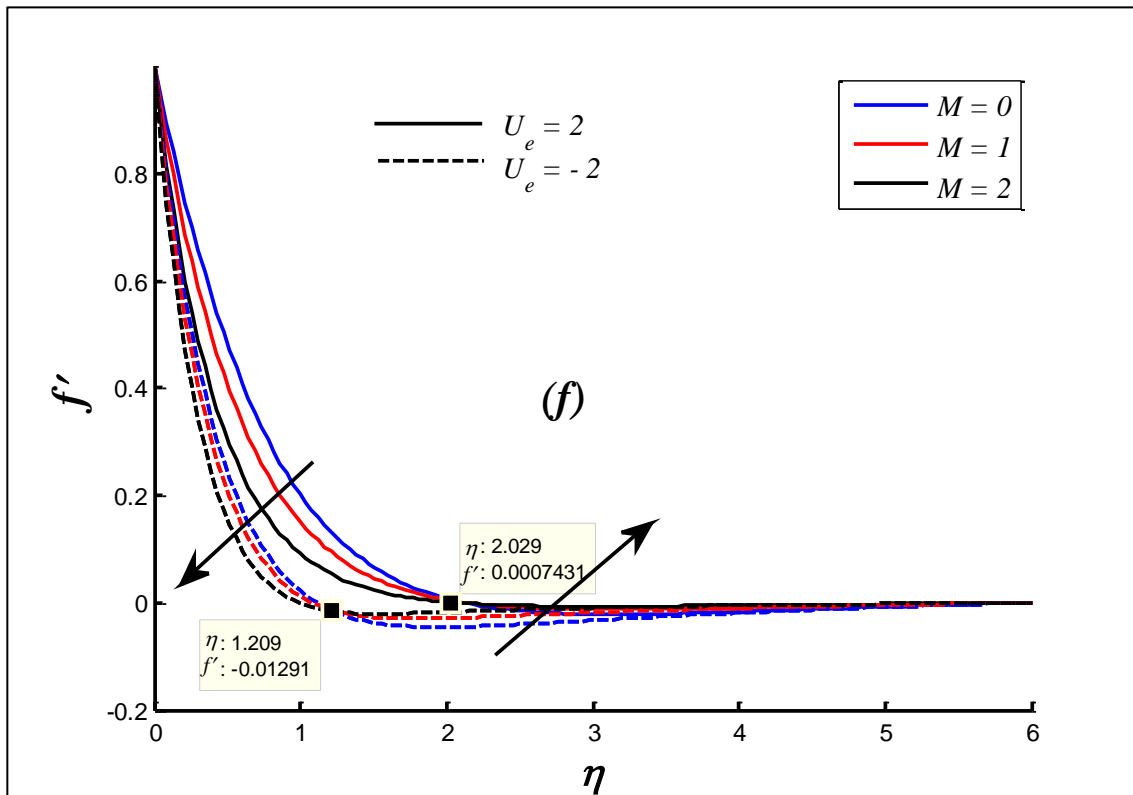
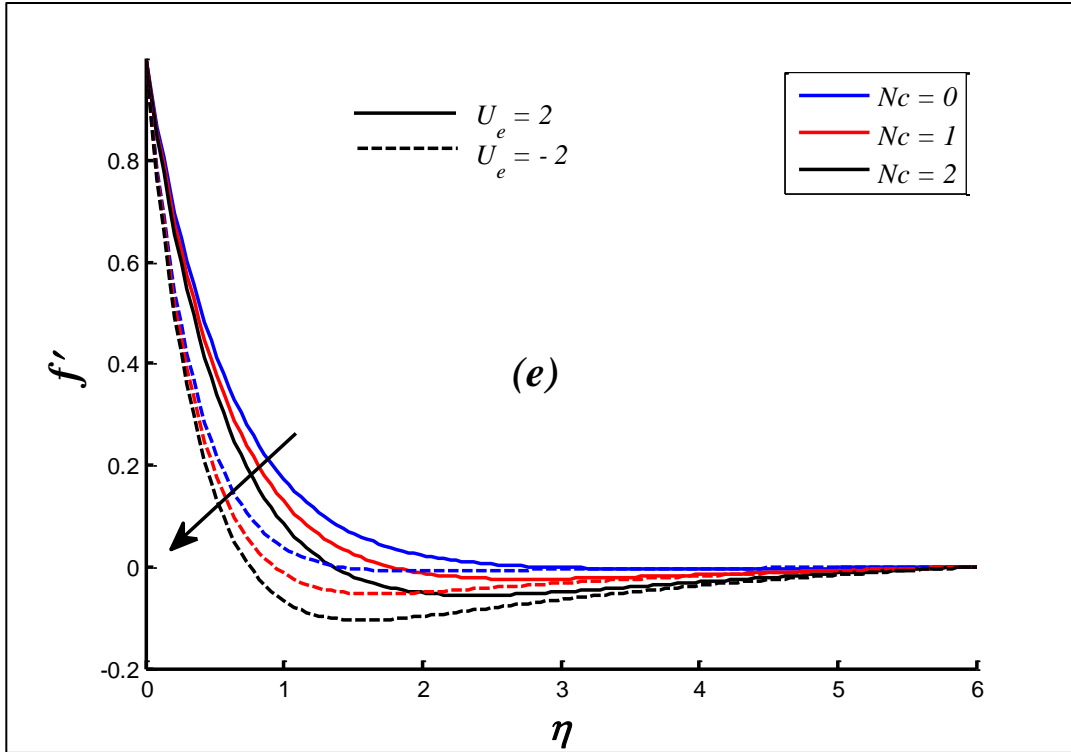
4. RESULTS AND DISCUSSION

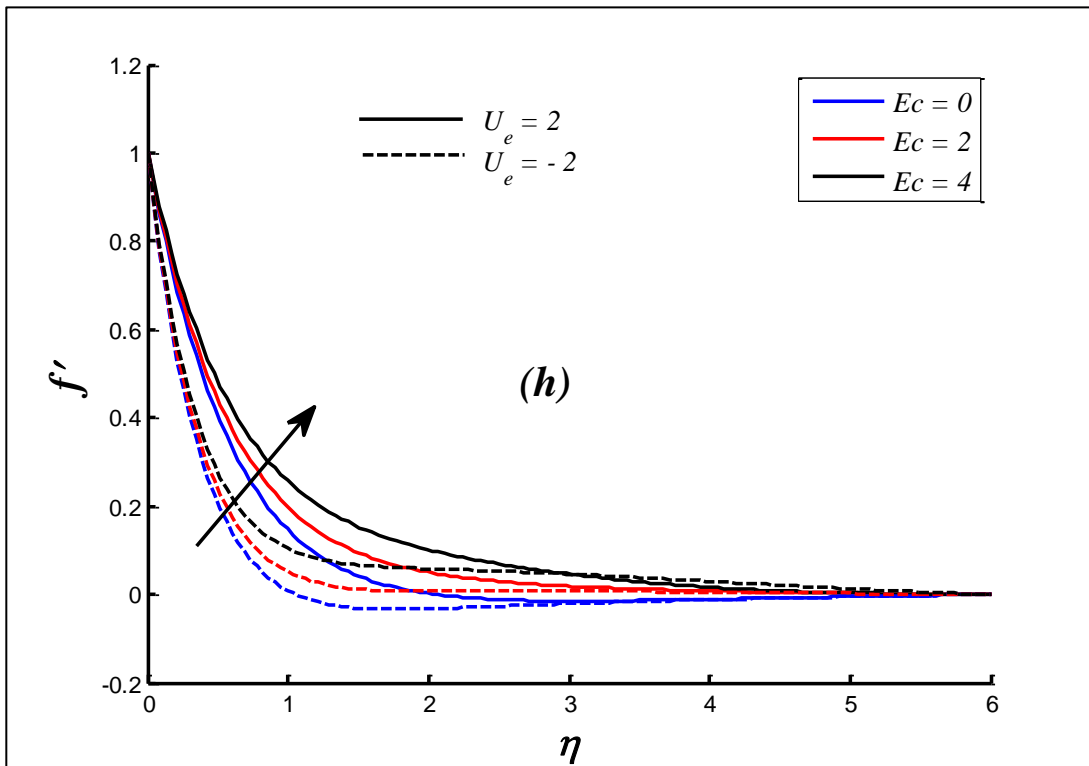
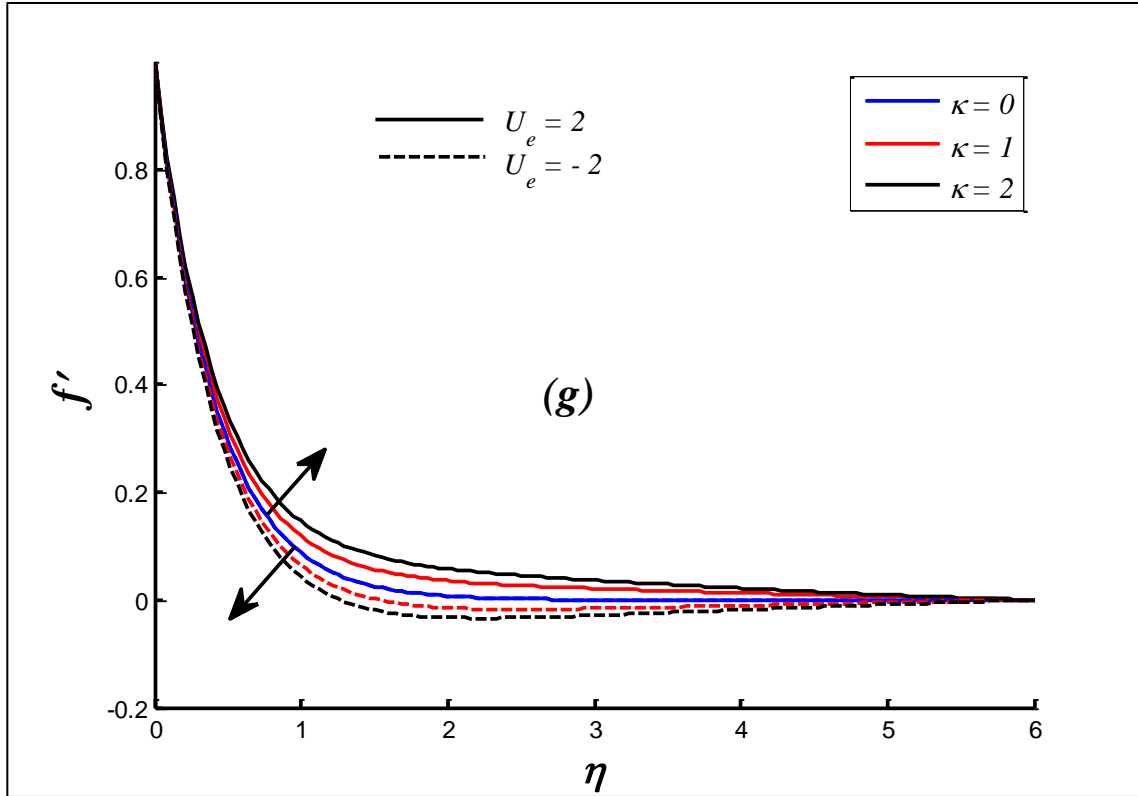
MATLAB computations are visualized in **Figs. 2-9** for the impact of selected parameters on the primary (axial) velocity, temperature, nanoparticle concentration and motile microorganism

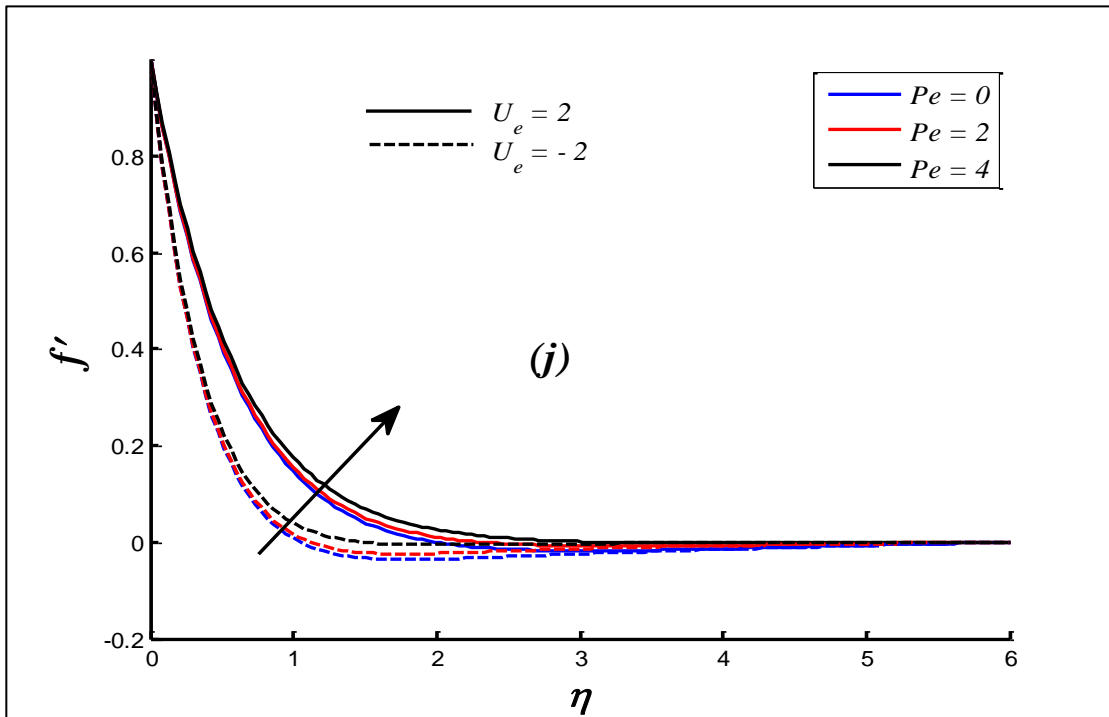
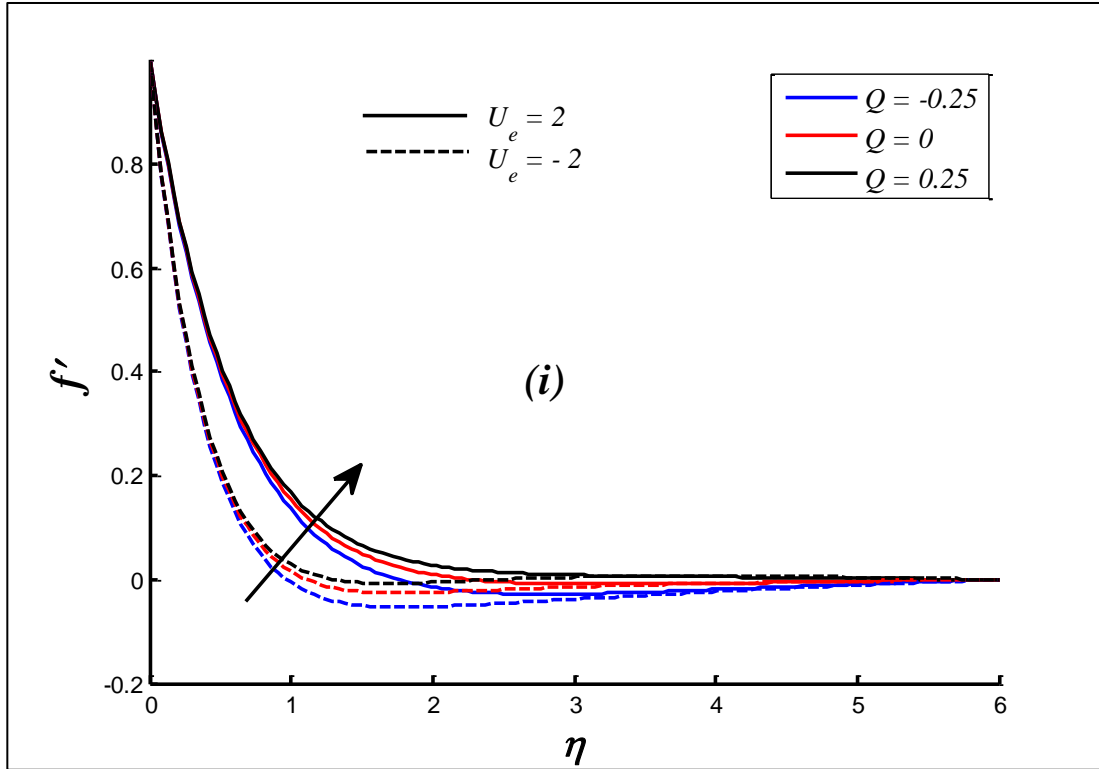
density number (concentration) distributions with transverse coordinate (η). This permits an appraisal of the interplay between different multi-physical effects in the non-Newtonian bio-nano electromagnetic functional coating boundary layer regime.



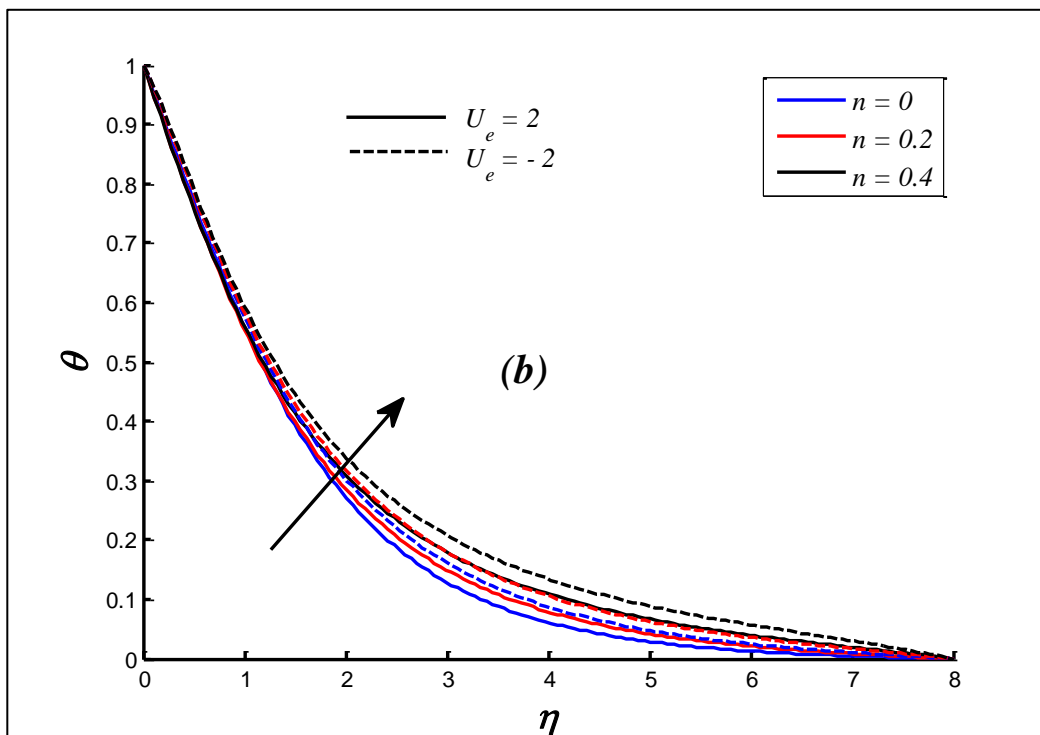
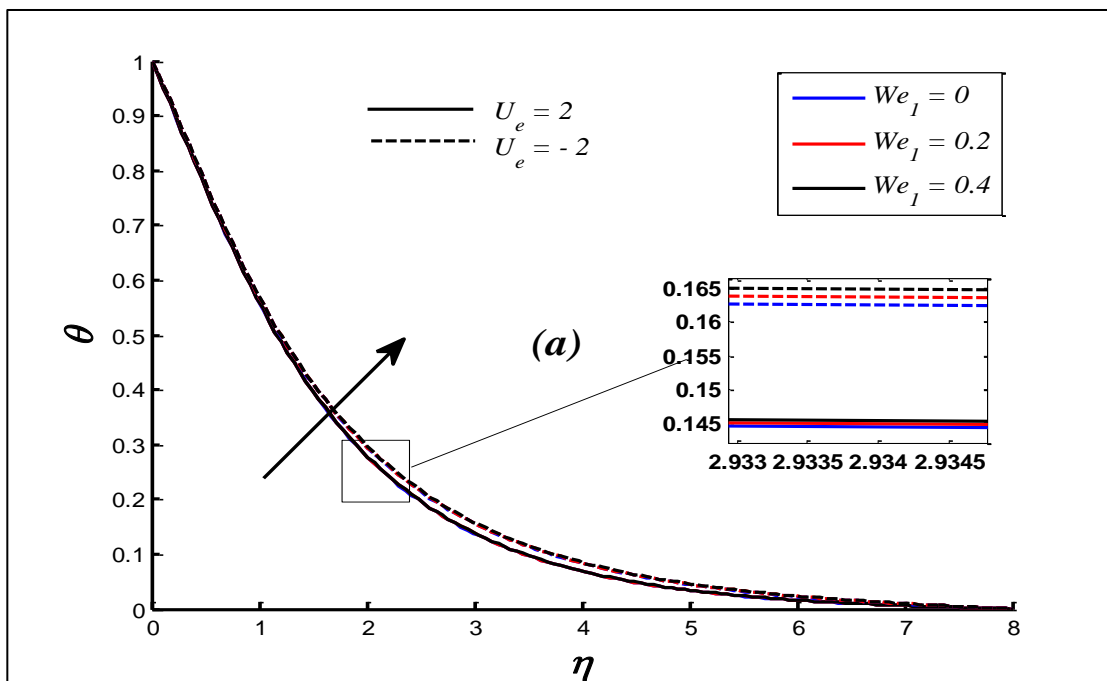


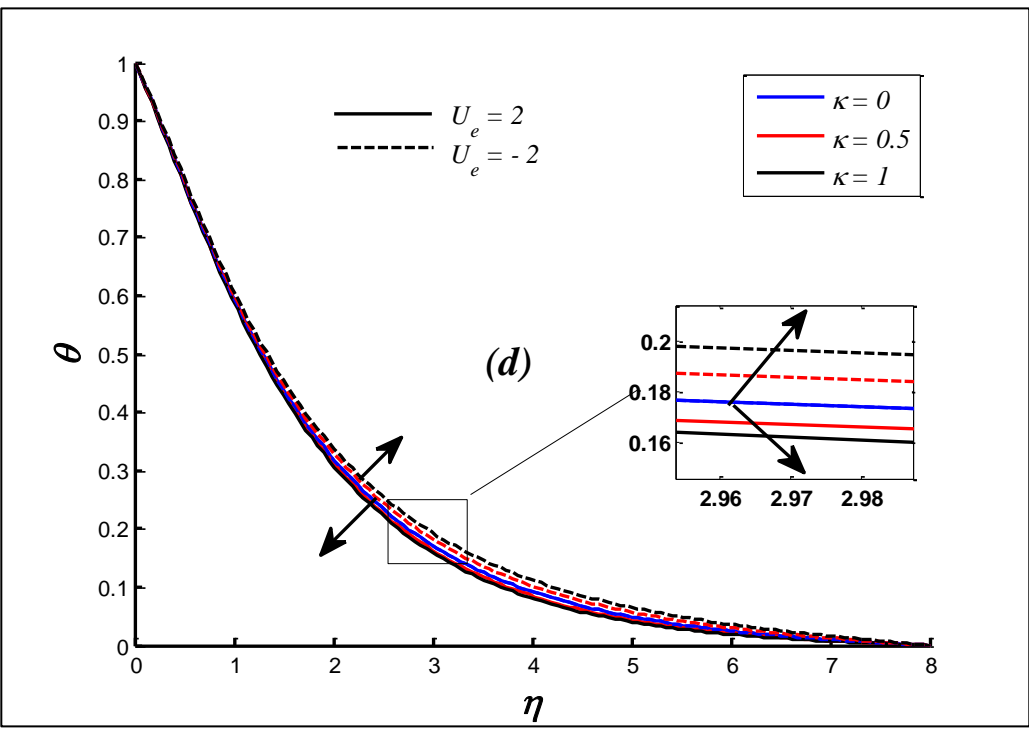
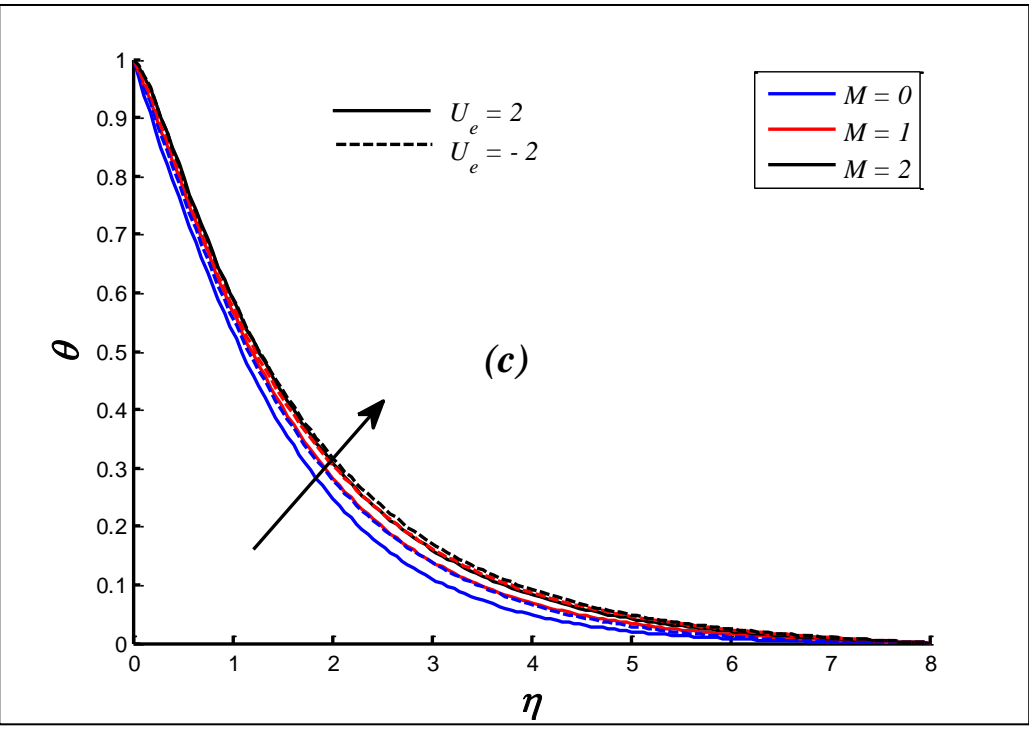


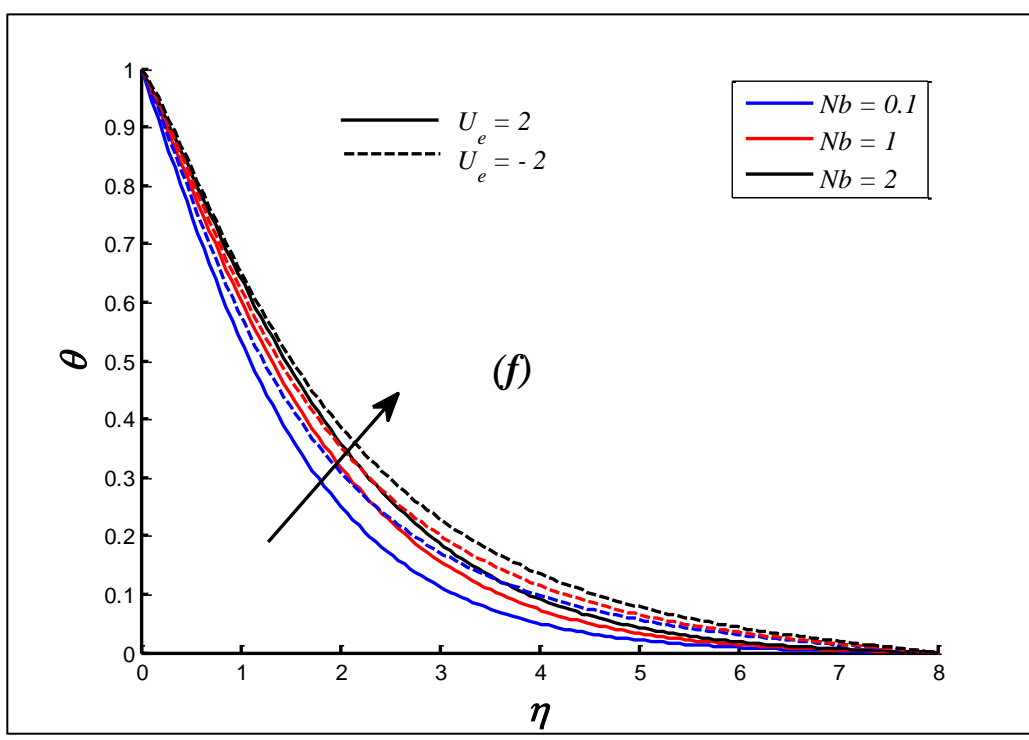
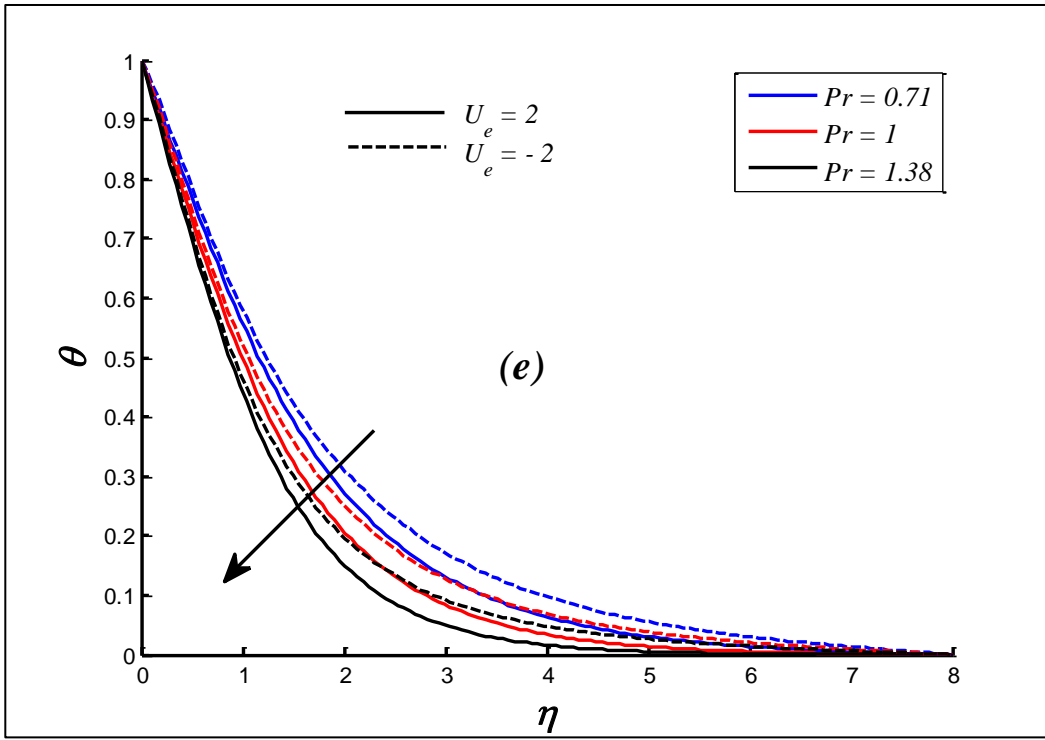


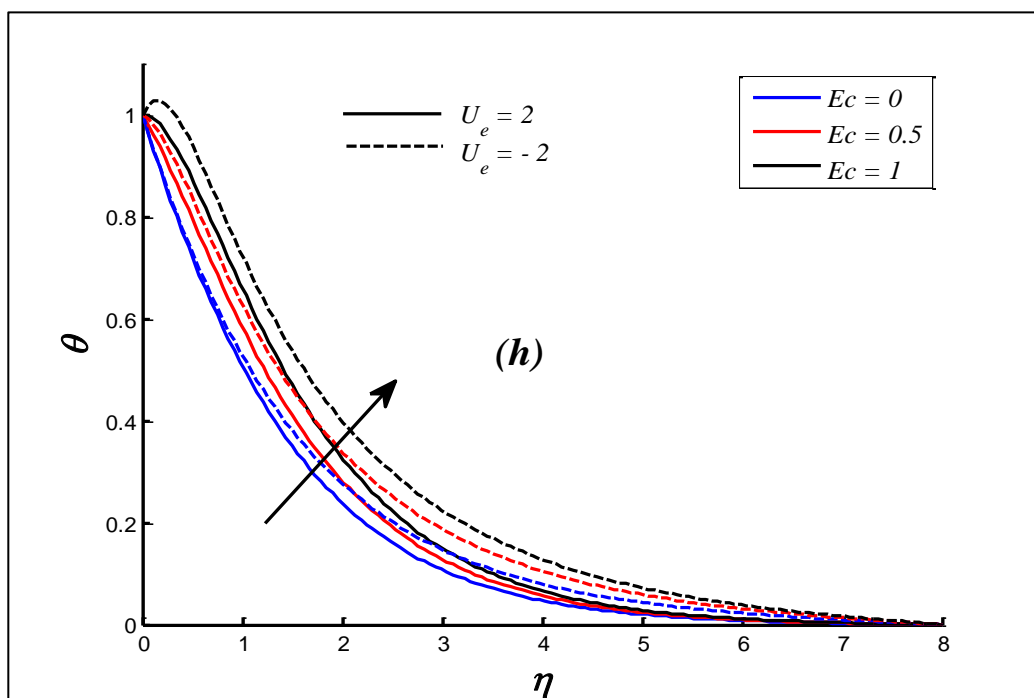
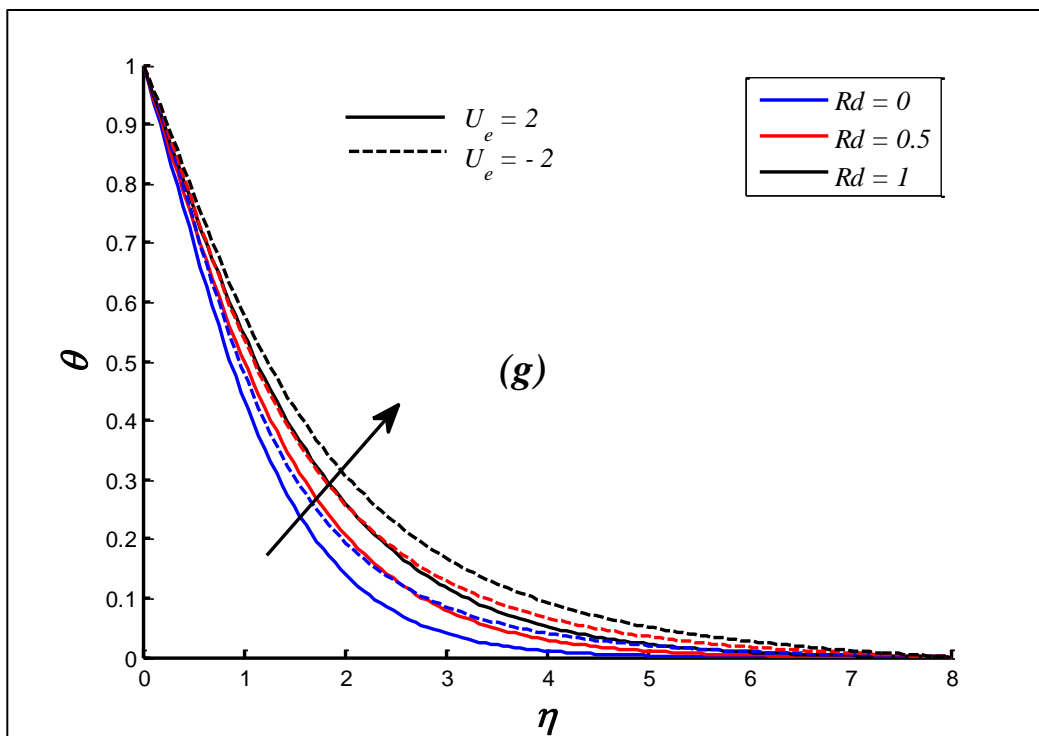


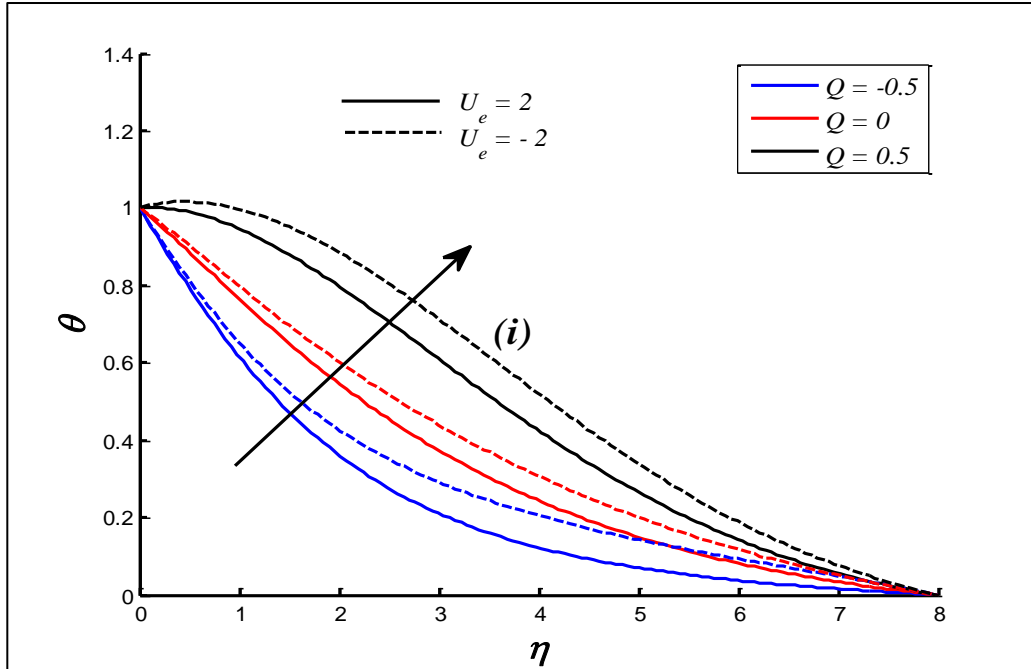
Figs.2(a-j) Effects of We_1 , n , λ , Nr , Nc , M , κ , Ec , Q and Pe on primary (axial) velocity f' versus η for the fixed parameter values of $\lambda = 0.1$; $Nr = 1$; $Nc = 1$; $Pr = 0.71$; $\Omega_r = 1$; $\Omega_c = 1$; $Ec = 1$; $Nb = Nt = 1$; $n = 0.3$; $We_1 = 0.1$; $We_2 = 0.2$; $\kappa = 2$; $M = 2$; $Q = -0.1$; $Rd = 1$; $Le = 1$; $Pe = 1$; $\Omega = 1$; $Lb = 0.2$; $\gamma = 0.5$ and $\xi = 0.5$.











Figs.3(a-i) Effects of $We_1, n, \lambda, Nr, Nc, M, \kappa, Ec, Q$ and Pe on nanoparticle temperature θ versus η for fixed parameter values of $\lambda = 0.3; Nr = Nc = 0.5; Pr = 0.71; \Omega_r = 0.1; \Omega_c = 0.1; Ec = 0.5; Nb = Nt = 1; n = 0.3; We_1 = 0.1; We_2 = 0.2; \kappa = 2; M = 1; Q = -0.5; Rd = 1; Le = 0.5; Pe = 0.5; \Omega = 1; Lb = 0.5; \gamma = 0.5$ and $\xi = 0.5$.

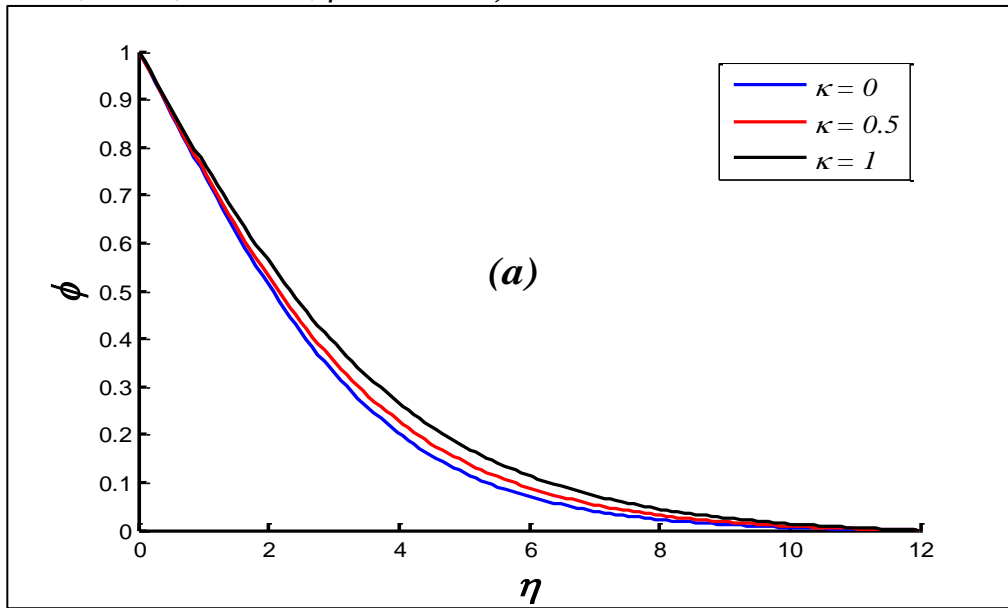


Fig.4(a) Effect of κ on nanoparticle concentration (φ) versus η for fixed parameter values of $\lambda = 0.1; Nr = 0.1; Nc = 1; Pr = 0.71; \Omega_r = 0.3; \Omega_c = 0.1; Ec = 1; U_e = 3; Nb = Nt = 0.5; n = 0.4; We_1 = 0.1; We_2 = 0.2; M = 0.1; Q = -1; Rd = 1; Le = 2; Pe = 1; \Omega = 0.1; Lb = 0.5; \gamma = 0.5$ and $\xi = 0.5$.

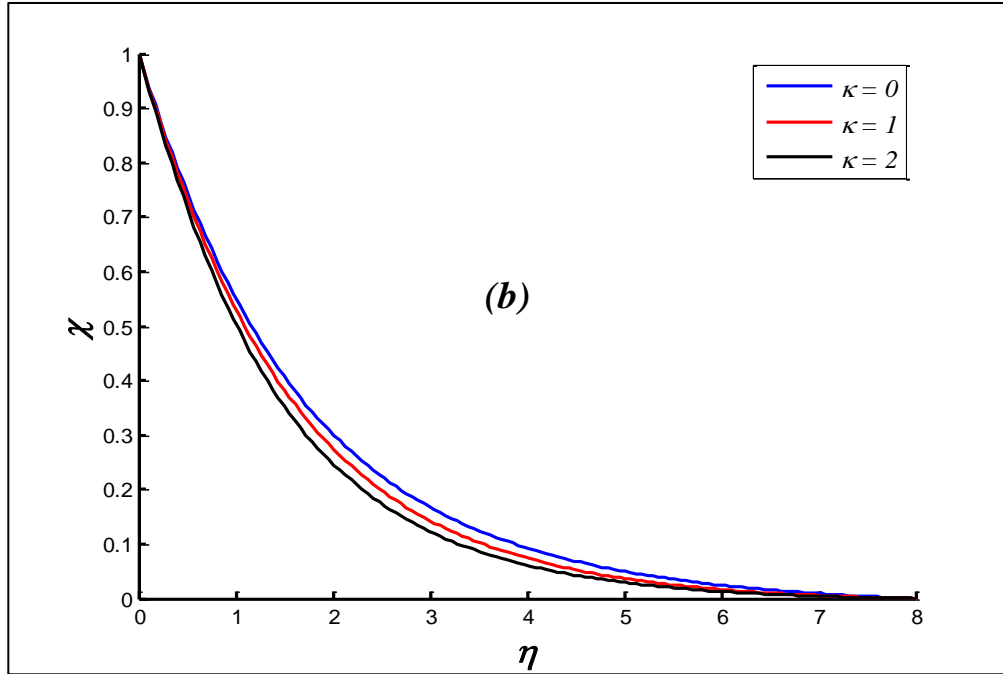


Fig.4(b) Effects of κ on number density (concentration) of the microorganisms (χ) versus η for fixed parameter values of $\lambda = 0.5$; $Nr = Nc = 0.5$; $Pr = 0.71$; $\Omega_r = 2$; $\Omega_c = 1$; $Ec = 0.5$; $U_e = 1$; $Nb = Nt = 1$; $n = 0.5$; $We_1 = 0.1$; $We_2 = 0.2$; $M = 1$; $Q = -0.2$; $Rd = 1$; $Le = 0.2$; $Pe = 0.5$; $\Omega = 1$; $Lb = 1$; $\gamma = 0.5$ and $\xi = 0.5$.

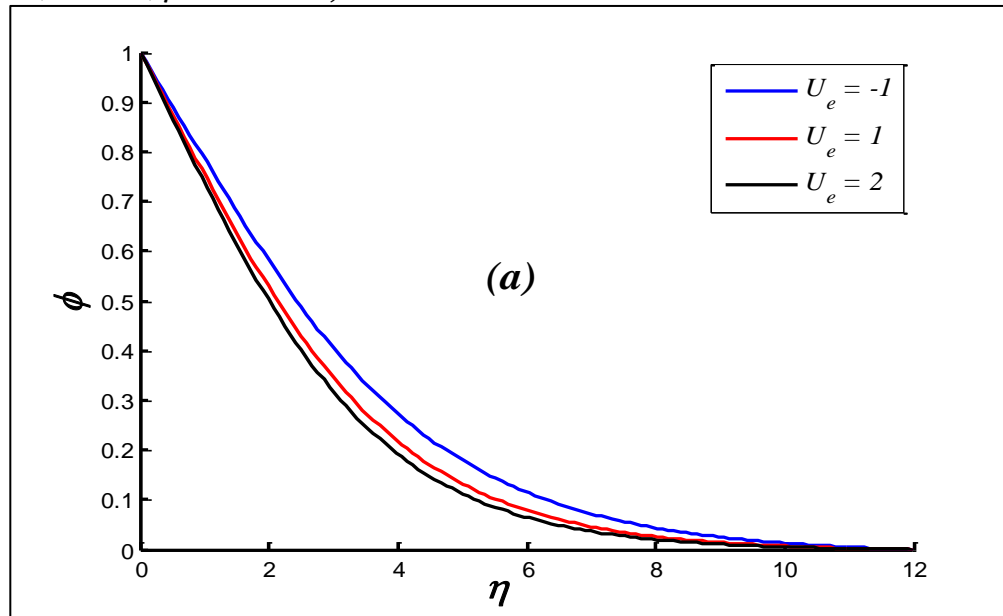


Fig.5(a) Effect of U_e on nanoparticle concentration (ϕ) versus η for fixed parameter values of $\lambda = 0.1$; $Nr = 0.1$; $Nc = 1$; $Pr = 0.71$; $\Omega_r = 0.3$; $\Omega_c = 0.1$; $Ec = 1$; $Nb = Nt = 0.5$; $n = 0.4$; $We_1 = 0.1$; $We_2 = 0.2$; $\kappa = 0.4$; $M = 1$; $Q = -1$; $Rd = 1$; $Le = 2$; $Pe = 1$; $\Omega = 0.1$; $Lb = 0.5$; $\gamma = 0.5$ and $\xi = 0.5$.

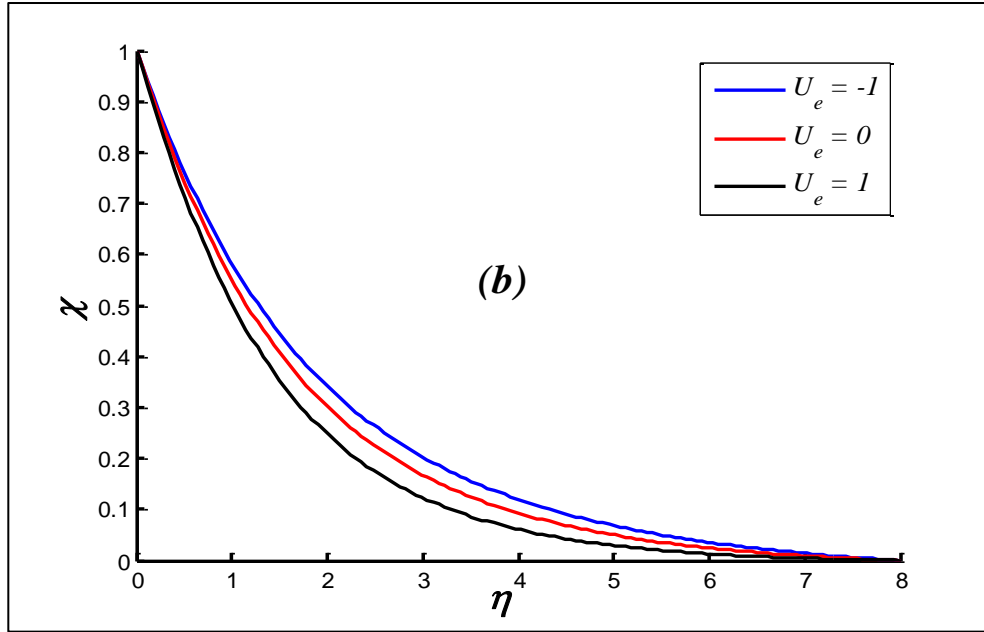


Fig.5(b) Effects of U_e on number density (concentration) of the microorganisms (χ) versus η for fixed parameter values of $\lambda = 0.5$; $Nr = Nc = 0.5$; $Pr = 0.71$; $\Omega_r = 2$; $\Omega_c = 1$; $Ec = 0.5$; $U_e = 1$; $Nb = Nt = 1$; $n = 0.5$; $We_1 = 0.1$; $We_2 = 0.2$; $M = 1$; $Q = -0.2$; $Rd = 1$; $Le = 0.2$; $Pe = 0.5$; $\Omega = 1$; $Lb = 1$; $\gamma = 0.5$ and $\xi = 0.5$.

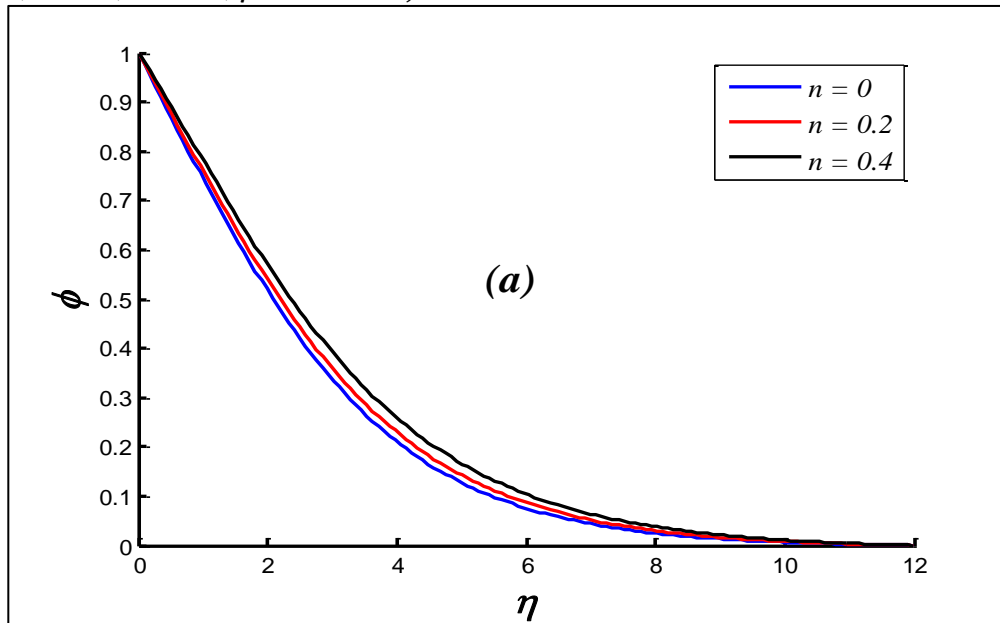


Fig.6(a) Effect of n on nanoparticle concentration (ϕ) versus η for fixed parameter values of $\lambda = 0.1$; $Nr = 0.1$; $Nc = 1$; $Pr = 0.71$; $\Omega_r = 0.3$; $\Omega_c = 0.1$; $Ec = 1$; $Nb = Nt = 0.5$; $We_1 = 0.1$; $We_2 = 0.2$; $\kappa = 0.4$; $M = 0.1$; $Q = -1$; $Rd = 1$; $Le = 2$; $Pe = 1$; $\Omega = 0.1$; $Lb = 0.5$; $\gamma = 0.5$ and $\xi = 0.5$.

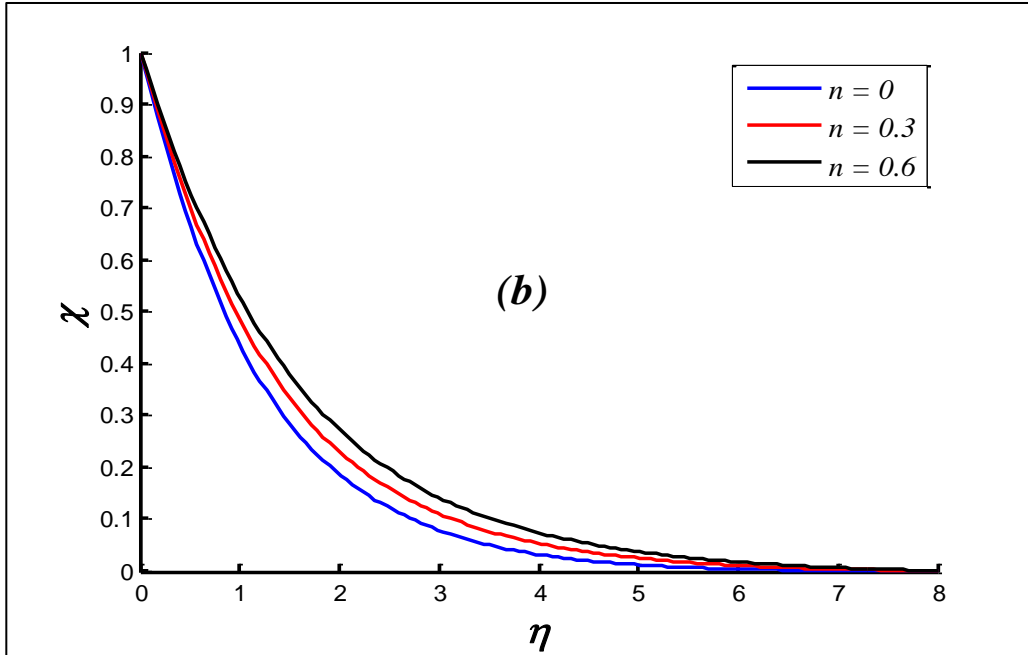


Fig.6(b) Effects of n on number density (concentration) of the microorganisms (χ) versus η for fixed parameter values of $\lambda = 0.5$; $Nr = Nc = 0.5$; $Pr = 0.71$; $\Omega_r = 2$; $\Omega_c = 1$; $Ec = 1.5$; $U_e = 1$; $Nb = Nt = 1$; $\kappa = 0.5$; $We_1 = 0.1$; $We_2 = 0.2$; $M = 1$; $Q = -0.2$; $Rd = 1$; $Le = 0.2$; $Pe = 0.5$; $\Omega = 1$; $Lb = 1$; $\gamma = 0.5$ and $\xi = 0.5$.

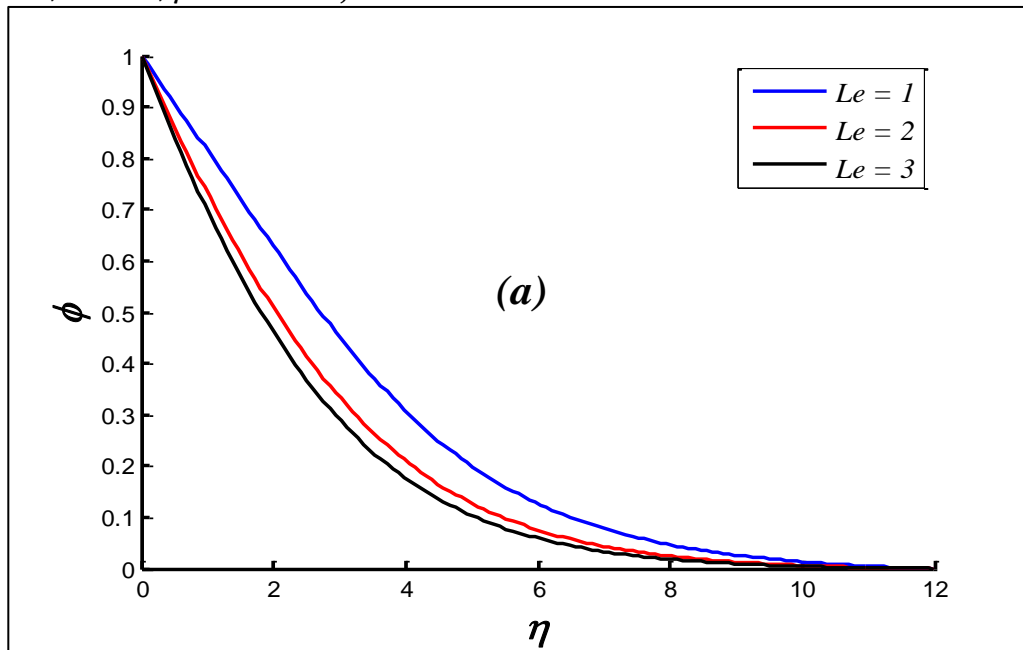


Fig.7(a) Effect of Le on nanoparticle concentration (ϕ) versus η for fixed parameter values of $\lambda = 0.1$; $Nr = 0.1$; $Nc = 1$; $Pr = 0.71$; $\Omega_r = 0.3$; $\Omega_c = 0.1$; $Ec = 1$; $U_e = 1$; $Nb = Nt = 0.5$; $n = 0.4$; $We_1 = 0.1$; $We_2 = 0.2$; $\kappa = 0.4$; $M = 0.1$; $Q = -1$; $Rd = 1$; $Pe = 1$; $\Omega = 0.1$; $Lb = 0.5$; $\gamma = 0.5$ and $\xi = 0.5$.

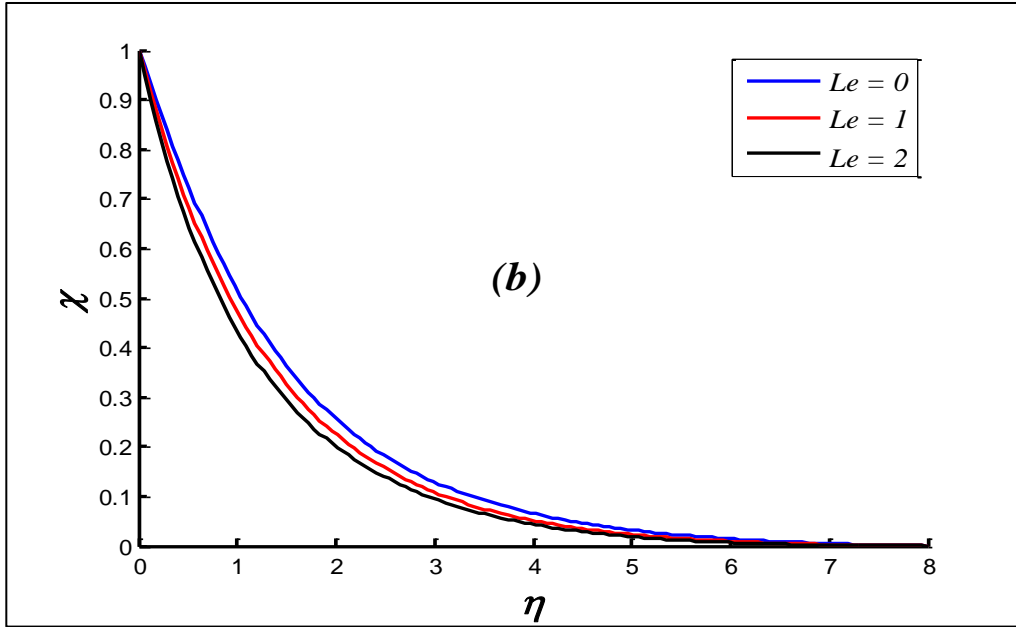


Fig.7(b) Effects of Le on number density (concentration) of the microorganisms (χ) versus η for fixed parameter values of $\lambda = 0.5$; $Nr = Nc = 0.5$; $Pr = 0.71$; $\Omega_r = 2$; $\Omega_c = 1$; $Ec = 0.5$; $U_e = 1$; $Nb = Nt = 1$; $n = 0.5$; $We_1 = 0.1$; $We_2 = 0.2$; $M = 1$; $Q = -0.2$; $Rd = 1$; $\kappa = 1$; $Pe = 0.5$; $\Omega = 1$; $Lb = 1$; $\gamma = 0.5$ and $\xi = 0.5$.

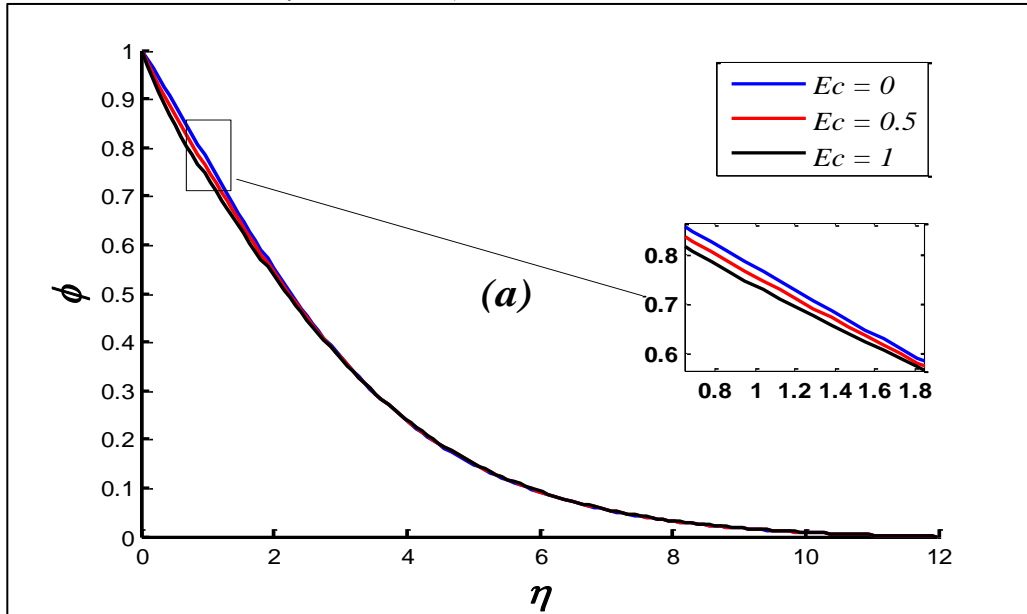


Fig.8(a) Effect of Ec on nanoparticle concentration (φ) versus η for fixed parameter values of $\lambda = 0.1$; $Nr = 0.1$; $Nc = 1$; $Pr = 0.71$; $\Omega_r = 0.3$; $\Omega_c = 0.1$; $Le = 2$; $U_e = 2$; $Nb = Nt = 0.5$; $n = 0.4$; $We_1 = 0.1$; $We_2 = 0.2$; $\kappa = 0.4$; $M = 0.1$; $Q = -1$; $Rd = 1$; $Pe = 1$; $\Omega = 0.1$; $Lb = 0.5$; $\gamma = 0.5$ and $\xi = 0.5$.

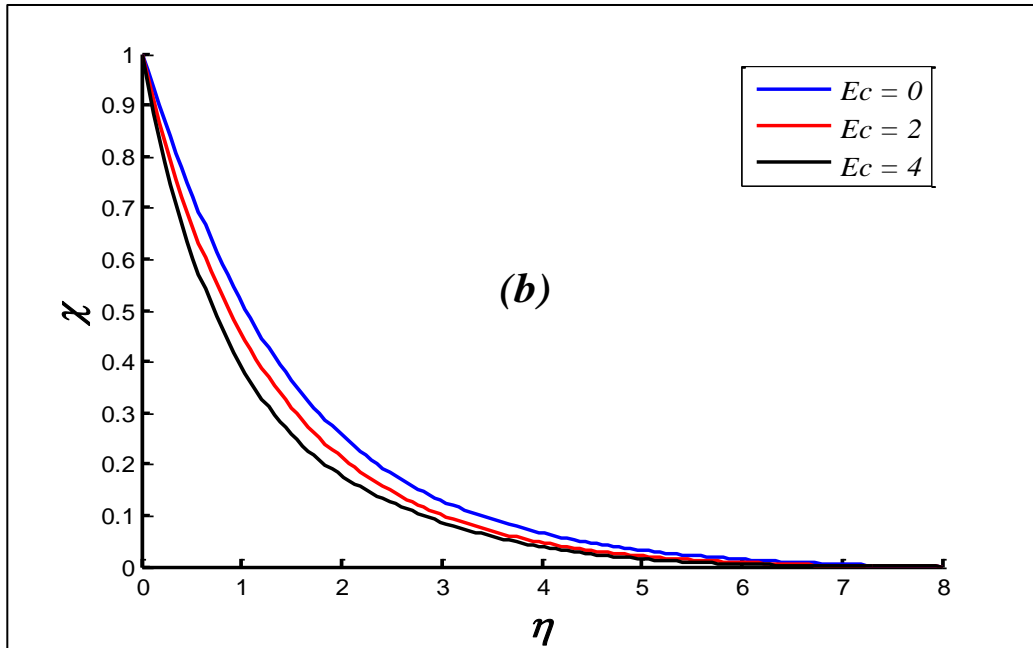


Fig.8(b) Effects of Ec on number density (concentration) of the microorganisms (χ) versus η for fixed parameter values of $\lambda = 0.5$; $Nr = Nc = 0.5$; $Pr = 0.71$; $\Omega_r = 2$; $\Omega_c = 1$; $Le = 0.2$; $U_e = 1$; $Nb = Nt = 1$; $n = 0.5$; $We_1 = 0.1$; $We_2 = 0.2$; $M = 1$; $Q = -0.2$; $Rd = 1$; $\kappa = 1$; $Pe = 0.5$; $\Omega = 1$; $Lb = 1$; $\gamma = 0.5$ and $\xi = 0.5$.

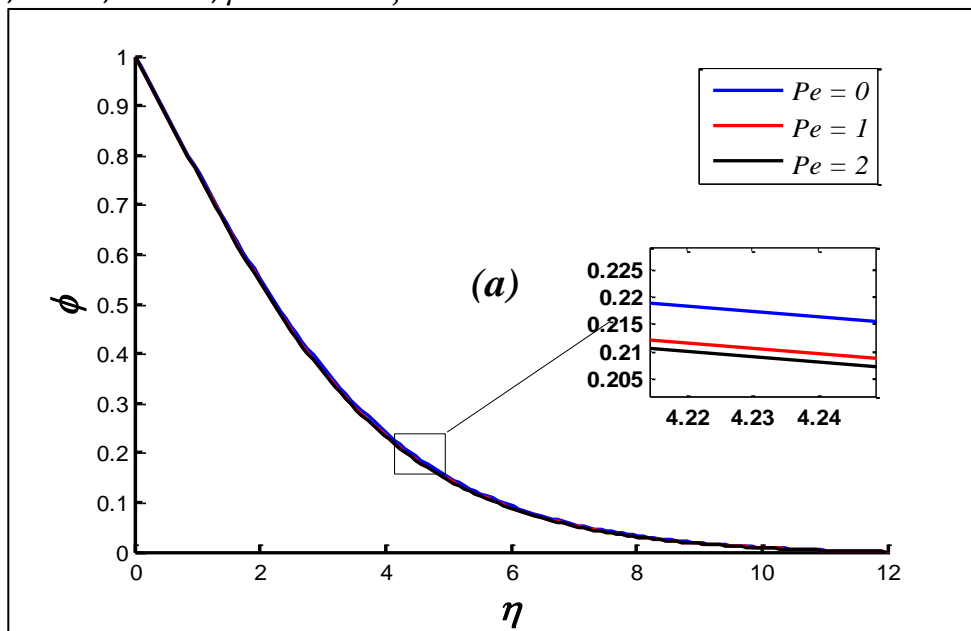


Fig.9(a) Effect of Pe on nanoparticle concentration (φ) versus η for fixed parameter values of $\lambda = 0.1$; $Nr = 0.1$; $Nc = 1$; $Pr = 0.71$; $\Omega_r = 0.3$; $\Omega_c = 0.1$; $Le = 2$; $U_e = 2$; $Nb = Nt = 0.5$; $n = 0.4$; $We_1 = 0.1$; $We_2 = 0.2$; $\kappa = 0.4$; $M = 0.1$; $Q = -1$; $Rd = 1$; $Ec = 1$; $\Omega = 0.1$; $Lb = 0.5$; $\gamma = 0.5$ and $\xi = 0.5$.

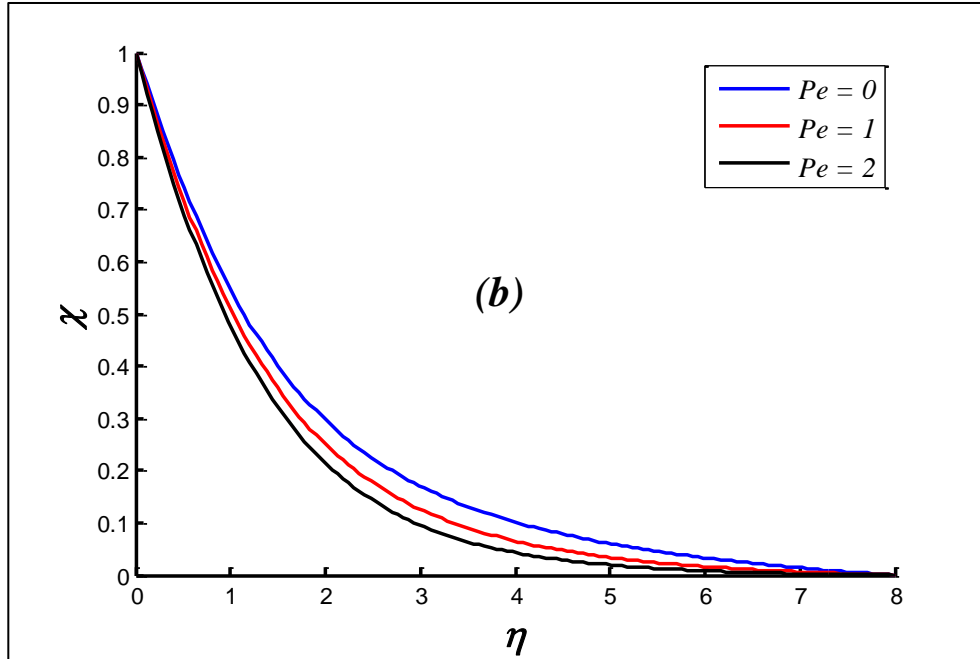


Fig.9(b) Effects of Pe on number density (concentration) of the microorganisms (χ) versus η for fixed parameter values of $\lambda = 0.5$; $Nr = Nc = 0.5$; $Pr = 0.71$; $\Omega_T = 2$; $\Omega_C = 1$; $Le = 0.2$; $U_e = 1$; $Nb = Nt = 1$; $n = 0.5$; $We_1 = 0.1$; $We_2 = 0.2$; $M = 1$; $Q = -0.5$; $Rd = 1$; $\kappa = 1$; $\Omega = 1$; $Lb = 1$; $\gamma = 0.5$ and $\xi = 0.5$.

Table 2: Numerical values for local (nanoparticle) Sherwood number $-\phi'(0)$ and local micro-organism density number $-\chi'(0)$ at the surface with various parameters at fixed values of $\lambda = 0.1$; $Nr = 0.1$; $Nc = 0.1$; $Pr = 0.71$; $Ec = 1$; $U_e = 0.5$; $Le = 0.5$; $We_2 = 0.2$; $Q = -0.5$; $Rd = 0.5$; $\Omega = 0.5$; $Lb = 0.5$; $\xi = 0.5$ and $\gamma = 0.5$.

Parameters									$-\phi'(0)$	$-\chi'(0)$
Nt	Nb	n	We_1	κ	M	Ω_C	Ω_T	Pe		
0	0.5	0.3	0.1	0.5	0.5	0.3	0.2	0.5	0.185096415488939	0.588877322174173
0.3									0.401905853782669	0.757109665874927
0.5									0.607577608254790	0.836204471754209
	0.1								1.083668416052490	2.633822739243599
	0.3								0.812475814792563	1.239615927557313
	0.5								0.607577608254790	0.836204471754209
		0.1							0.587791930915069	0.707908996945013
		0.2							0.627897446768081	0.908029576461113
		0.3							0.712848860281543	0.955630559135686

			0					1.123902613676399	1.320397653838180
			0.1					0.607577608254790	0.836204471754209
			0.2					0.470372442742222	0.801269864583848
				0.5				0.607577608254790	0.836204471754209
				0.6				0.627822759873900	0.838069304588296
				0.7				0.695722777622285	0.951278135403397
					0.3			0.491354711721586	0.624187832093254
					0.5			0.607577608254790	0.836204471754209
					0.7			0.924339575400912	1.096544198914611
						0		2.839287993189002	13.331716175384789
						0.3		0.404262802461833	0.735032439485112
						0.6		0.324736262033513	0.569290414285967
							0.1	1.318186993364106	1.151492360849763
							0.2	0.607577608254790	0.836204471754209
							0.3	0.218025273561929	0.251538692577106
							0	0.729841391437787	0.513261691592435
							0.5	0.607577608254790	0.836204471754209
							1	0.581560765490280	0.968052193096578

Fig.2(a - j) illustrate for the case of positive and negative values of the electric field parameter (U_e), the effects of non-Newtonian parameters (axial Weissenberg number i.e. We_1 and power law parameter, n), mixed convection parameter (λ), buoyancy ratio parameter (Nr), Rayleigh bioconvection number (Nc), magnetic interaction number (M), electroosmosis parameter (κ), Eckert number (Ec), heat generation/absorption parameter (Q) and bioconvection Péclet number (Pe), on the axial (primary) velocity distributions. It is important to note that in the plots, two values are studied for electric field parameter U_e since the electrical field orientation is critical in controlling the transport phenomena in the stretching charged ionic nanofluid coating. When the axial electric field is aligned in the positive axial direction (as shown in Fig. 1), U_e i. e. electrical field parameter value is *negative*, whereas when the axial electric field is aligned in the reverse (negative) axial direction, the U_e parameter value is *positive*. The axial velocity evolution with variation in We_1 is shown in Fig 2a for both $U_e > 0$ and $U_e < 0$. Axial Weissenberg number, $We_1 = \sqrt{\frac{2a}{v_f}} a\bar{X}\Gamma$ represents the *ratio of the relaxation time of the nanofluid to the time scale of the flow*. In rheological coatings, relaxation time quantifies the time it takes one portion of the polymer

entanglement network to react to alterations in another portion and is therefore a nonlinear memory effect. It is also a measure of the elastic force to the viscous force in the fluid. The axial Weissenberg number features in the shear-modified terms in the primary (axial) momentum Eqn. (22), $(nWe_1f'' + (1 - n))f'''$. Intensification in We_1 damps the axial velocity and increases the momentum boundary layer thickness. Higher values of We_1 corresponds to the relaxation time exceeding the time scale of a flow and greater viscous effects. This manifests in strong retardation in the flow. The opposite scenario of low values of We_1 correspond to the time scale of the flow exceeding the relaxation time and the dominance of elastic force over viscous force. This produces acceleration and greater axial velocity. In the case where $We_1 = 0$, viscoelasticity vanishes, and the maximum axial velocity is observed. The trends are sustained throughout the boundary layer domain. Furthermore, with $U_e > 0$ i.e. for which the electric field is aligned in the reverse (negative) axial direction, consistently greater magnitudes of axial velocity are computed compared with the case when $U_e < 0$ (positively aligned axial electrical field) and the disparity is greatest in the vicinity of the wall. Asymptotically smooth profiles are computed in the free stream confirming that an adequately infinity boundary condition has been prescribed in the MATLAB computations. Fig. 2(b) shows the effect of the power law index number (n) on the axial velocity profile for both $U_e > 0$ and $U_e < 0$. The maximum axial velocity is found when the power law index number assumes zero value i. e. Newtonian fluid, and this behaviour is computed for both negative and positive electric field parameters, although significantly greater magnitudes are observed for $U_e > 0$. For increasingly pseudoplastic behaviour, i. e. increment in the values of n , there is a strong deceleration in axial flow and a thicker momentum boundary layer is produced. The implication is that stronger shear-thinning behaviour of the nanofluid damps the velocity and there is a significant modification in the viscosity with increasing shear rate. A characteristic aspect of non-Newtonian fluids is the decrease in shear rate (compared to Newtonian fluids). With intensification in shear thinning (pseudoplasticity), the fluid particles gradually align with the streamlines, an alignment that changes almost instantaneously in response to changes in imposed shear; after complete alignment at high shear, the apparent viscosity remains constant. Clearly the inclusion of the tangent hyperbolic model in the simulation produces a velocity distribution which significantly deviates from the conventional Newtonian model. The pseudoplastic behaviour of nanofluids has also been identified experimentally by Choi and co-workers [11-13]. In Fig. **Fig.2(c)**, it is evident that increasing values of mixed convection parameter substantially deplete

the primary (axial) velocity. Auxiliary flow (heated wall) and forced convection flow are represented by the cases $\lambda > 0$ and $\lambda = 0$. This parameter features in the terms, $+\lambda(\theta - Nr\varphi - Nc\chi)$ in Eqn. (22) and for the mixed convection case, $\lambda > 0$, enables the temperature, nanoparticle concentration and micro-organism fields to influence the primary momentum. Clearly the boundary layer equations for heat, nanoparticle concentration and microorganism density number are strongly coupled to the primary momentum (velocity) field via these terms. For the *forced* convection case, $\lambda = 0$, these terms vanish. The two cases of $U_e > 0$ and $U_e < 0$ are again considered and higher velocity magnitudes are produced for the former. An increase in the mixed convection parameter suppresses axial momentum development in the stretching regime. It inhibits the momentum transfer and leads to a thicker momentum boundary layer. Fig. 2 (d) and Fig. 2 (e) show the influence of the buoyancy ratio parameter (Nr) and the bioconvection Rayleigh number (Nc) for mixed convection ($\lambda > 0$) on the axial velocity profile for the two electrical field cases $U_e > 0$ and $U_e < 0$. A significant suppression in axial (primary) velocity profiles is induced with an increment in both buoyancy force parameters (Nr, Nc). Maximum axial velocity (minimal momentum boundary layer thickness) arises when $Nc = Nr = 0$ i. e. in the absence of the buoyancy forces. Both buoyancy parameters feature as linear coupling terms in the primary momentum Eqn. (22), $+\lambda(\theta - Nr\varphi - Nc\chi)$ and exert a marked influence on momentum development in the boundary layer. Again, substantially greater axial velocity is computed for $U_e > 0$ compared with $U_e < 0$. Effectively the axial flow is strongly damped with intensification in buoyancy forces and this has also been reported in other studies of nanofluid bioconvection including [45] and [49]. Fig. 2(f) reveals that with an increment in magnetic parameter, M there is a prominent reduction in axial velocity. $M = \frac{\sigma^* B_0^2}{a\rho_f}$ and expresses the ratio between electromagnetic force (Lorentz drag) and inertia force. Increasing magnetic field B_0 counteracts the mobility of the fluid in the initial phase ($0 \leq \eta \leq 1.209$) when the electric field is negative and ($0 \leq \eta \leq 2.029$) when the electric field is positive. When the magnetic interaction number is increased, the velocity profile shows a decreasing tendency in the initial phase. As an increase in magnetic interaction number M leads to an increase in drag force, the velocity of the fluid decreases due to the increased drag force. Axial velocity is clearly therefore maximized in the regime with $M = 0$ i. e. for the non-magnetic case, in which the momentum boundary layer thickness is minimized. As in other plots, the assistive electrical field scenario i.e. $U_e > 0$ produces greater axial velocity magnitudes

compared with the inhibitive electrical field scenario, $U_e < 0$. In the latter case, slightly negative values are observed at intermediate distances from the wall, indicating that for strong magnetic field and counteracting electrical field, there is a weak back flow in the regime.

Fig. 2 (g) shows the effect of the electroosmotic parameter (κ) on the axial fluid velocity, again for $U_e > 0$ and $U_e < 0$. It is again evident that higher axial (primary) velocity values are generated when the electric field parameter $U_e > 0$, as noted earlier, due to the reversed electrical field assisting the momentum development. The parameter κ is defined by $\kappa^2 = m^2 \frac{v_f}{a}$ (in which $m^2 =$

$-\frac{2\bar{z}^2 e^2 n_0}{\epsilon_{eff} k_B T_v}$ is the Debye-Hückel parameter). It features only in the electrical potential Eqn. (27) in

the term, $-\kappa^2 \sinh(\Phi)$. The electrical potential coupling term in Eqn. (22) i. e. $+U_e \Phi''$ enables

the primary momentum to be directly influenced by the electroosmotic parameter, κ . When the electroosmotic parameter is decreased, the electrical double layer thickness (EDL) is expanded and the intensity of collisions between particles on the extended surface increases. As, κ is increased, axial velocity is elevated for the $U_e > 0$ case whereas the opposite effect i. e. deceleration is produced for the $U_e < 0$ case. This behaviour is sustained throughout the regime i.e. at all values of η . A different modification in axial (primary) flow and boundary layer thickness is therefore induced with greater electroosmotic effect, depending on the orientation of the axial electrical field. This permits designers to manipulate the momentum characteristics in nano-coating manufacture via controlling the electrical field direction and also the electrical double layer (EDL) thickness. Fig.2(h) shows the effects of varying the Eckert number on the axial velocity profile of the fluid for both electrical field cases, $U_e > 0$ and $U_e < 0$. The Eckert number is used to describe the effects of self-heating of a fluid as a result of kinetic energy dissipation effects. It is found that the minimum axial fluid velocity occurs when viscous dissipation is absent ($Ec = 0$) for both cases of $U_e > 0$ and $U_e < 0$. However as observed in other plots, generally the magnitudes are greater for the assistive axial electrical field situation ($U_e > 0$) relative to the opposing electrical field situation ($U_e < 0$), although further from the wall there is a cross-over in behaviour. With an increase in the Eckert number, there is an increase in collisions between the fluid molecules. $Ec =$

$\frac{U_w^2}{c_p(T_w - T_\infty)}$ and features in both the conventional viscous heating term, $+(1 - n)Ec f''^2$ in the energy Eqn. (24) and also the magnetic Joule heating (Ohmic dissipation) term, $+M Pr E c f'^2$. The effect of Ec is therefore prominent on axial velocity since these terms are coupled with the primary

axial velocity. The Eckert number is used to describe the effects of self-heating of a fluid as a result of kinetic energy dissipation effects. It is found that the minimum axial fluid velocity occurs when viscous dissipation is absent ($Ec = 0$) for both cases of $U_e > 0$ and $U_e < 0$. However as observed in other plots, generally the magnitudes are greater for the assistive axial electrical field situation ($U_e > 0$) relative to the opposing electrical field situation ($U_e < 0$), although further from the wall there is a cross-over in behaviour. With an increase in the Eckert number, there is an increase in collisions between the fluid molecules. $Ec =$

momentum Eqn. (22). In the boundary layer, the dissipation rate increases, leading to an increase in the axial velocity and strong acceleration in the flow. Fig. 2(i) depicts the effects of the heat sink/source (Q) on the axial fluid velocity for $U_e > 0$ and $U_e < 0$. An increase in the strength of the heat source ($Q > 0$) leads to an increase in the axial fluid velocity, whereas an increase in the strength of the heat sink ($Q < 0$) leads to a decrease in the axial fluid velocity. Heat source corresponds to energy generation in the nanofluid whereas heat sink implies energy absorption i.e. removal. Temperature is therefore strongly affected by $Q = \frac{Q_0}{\alpha \rho c_p}$, which appears in the linear term, $+Pr Q \theta$ in the energy Eqn. (24). Fig. 2(j) illustrates the effect of the bioconvection Péclet number, on the axial fluid velocity for both electric field parameter scenarios, i. e. $U_e > 0$ (*assistive electrical field*) and $U_e < 0$ (*inhibiting electrical field*). $Pe = \frac{\bar{b}W_c}{D_m}$ and arises in the terms, $-Pe(\chi' \varphi' + (\Omega + \chi)\varphi'')$ in the motile micro-organisms density number (concentration) boundary layer Eqn. (27). However coupling with the primary momentum Eqn. (22) (and secondary momentum Eqn. (23)) is achieved via the terms, $+Lb(f + g)\chi'$ also appearing in Eqn. (27). In an advection-dominated distribution, a high Pe value indicates advection, while a low Pe indicates diffusive flow. This parameter is also inversely proportional to the micro-organism diffusivity (D_n) whereas it is directly proportional to W_c (maximum swimming velocity of a micro-organism cell movement) and b (chemotaxis constant). Higher Pe values therefore indicate a lower micro-organism diffusivity and a higher micro-organism swimming velocity. The latter produces acceleration in the axial flow and explains the significant boost in axial (primary) velocity throughout the regime. The case $Pe = 0$ implies the micro-organisms are stationary i. e. not self-propelling and leads to a minimization in axial velocity magnitudes. Doping the nanofluid with gyrotactic micro-organisms can therefore be successfully exploited to manipulate flow characteristics in the coating regime.

Fig. 3(a-i) shows the dimensionless temperature (θ) distributions for various selected parameters, the $We_1, n, \lambda, Nr, Nc, M, \kappa, Ec, Q$ and Pe on nanoparticle versus η for again for both positive and negative values of the electric field parameter i.e. $U_e > 0$ (*assistive electrical field*) and $U_e < 0$ (*inhibiting electrical field*). Fig. 3(a-b) shows that increasing both rheological parameters (axial Weissenberg numbers We_1 , and power law index parameter n) results in a weak and stronger increase in temperature. Temperature at the stretching surface (wall) is therefore lowest for Newtonian fluid ($We_1 = n = 0$). Increasing elastic and decreasing viscous force (We_1 expresses the

ratio of elastic to viscous forces) and greater pseudoplastic behavior (higher n values) in the nanofluid therefore generates a heating effect and increases thermal boundary layer thickness, although the effect is more prominent for the latter. The inclusion of rheological parameters clearly produces significant deviation from the Newtonian case. Higher temperature magnitudes are observed for $U_e < 0$ (*opposing electrical field*) and $U_e > 0$ (*assisting electrical field*) which is the opposite effect to that for the axial velocity field computed earlier. Fig. 3(c-d) visualize the impact of magnetic interaction number, M , and electroosmotic parameter (κ) on temperature evolution, for $U_e < 0$ (*opposing electrical field*) and $U_e > 0$ (*assisting electrical field*) scenarios. It is observed that the temperature distribution increases uniformly when the magnetic interaction number is increased for both $U_e < 0$ and $U_e > 0$, although clearly greater temperatures are computed for $U_e < 0$ (*opposing electrical field*). The minimum temperature profile of the nanoparticles is generated for both negative and positive values of the electric field parameters for vanishing magnetic interaction number ($M = 0$), where no magnetic field is applied to the stretching sheet (see Fig. 3(c)). Fig. 3(d) shows that the temperature of the nanoparticles increases significantly when the electroosmotic parameter (κ) is elevated for the $U_e < 0$ case; the contrary trend is computed for $U_e > 0$ case. In other words, for reversed axial electrical field, greater κ or decreasing electrical Double layer thickness, heating in the boundary layer is produced, whereas for an aligned electrical field the opposite effect (cooling) is generated. Thermal boundary layer thickness is therefore accentuated with greater κ for $U_e < 0$ whereas it is depleted for $U_e > 0$. Smooth convergence of temperature profiles is achieved in the free stream in all temperature plots verifying that a sufficiently large infinity boundary condition has been adopted in the MATLAB bvp4c simulations. Overall, the temperature in the stretching nanofluid sheet can be manipulated successfully with the careful combination of applied transverse magnetic and axial electric fields. The effect of Prandtl number Pr on the nanoparticle temperature profile is shown in Fig. 3(e) for both $U_e < 0$ (*opposing electrical field*) and $U_e > 0$ (*assisting electrical field*) situations. Increasing the Prandtl number decreases the nanoparticle temperature in the regime, as shown in Fig. 3(e). A higher Prandtl number indicates a lower thermal conductivity of the electromagnetic rheological nanofluid, and this reduces the intensity of thermal diffusion in the boundary layer. Pr values of and above unity value are representative of metallic nanoparticle doped aqueous ionic nanofluids and electroconductive nanogels [61]. Increment in Pr also suppresses thermal boundary layer thickness. Momentum diffusivity relative to thermal diffusivity is also expressed in the Prandtl

number. An increase in Pr corresponds to a significant reduction in thermal diffusivity, which restricts molecular conduction in the nanofluid coating and cools the regime. Therefore, when it comes to managing temperature distributions, the precise selection of the thermal characteristics of the nanofluid is essential. Larger temperatures are also observed again for $U_e < 0$ (*opposing electrical field*) compared with $U_e > 0$ (*assisting electrical field*), confirming that electrical field orientation is also instrumental in regulating temperatures in the boundary layer.

Temperatures in the boundary layer domain rise with an increase in the Brownian parameter, Nb , as shown in Fig. 3(f). For higher Nb , the random mobility of nanoparticles in the material increases, leading to an intensification in ballistic collisions which generates more heat. As a result, the temperature of the nanofluid increases. In the Buongiorno model [14], larger Nb implies smaller diameter nanoparticles and smaller Nb corresponds to larger nanoparticles. Chaotic motions are therefore exacerbated with an increment in Nb . Nb features in the $+Pr Nb \theta' \varphi'$ term in the energy (thermal) boundary layer Eqn. (24) and the in the term, $+\frac{Nt}{Nb} \theta''$ nanoparticle concentration boundary layer Eqn. (25). There is evidently a strong interplay between diffusive motion of the nanoparticles and the temperature field. Higher magnitudes of temperature are again associated with $U_e < 0$ (*opposing electrical field*) compared with $U_e > 0$ (*assisting electrical field*). The effects of the thermal radiation parameter (Rd) on $\theta(\eta)$ are shown in Fig. 3(g) for both electrical field cases $U_e < 0$ (*opposing*) and $U_e > 0$ (*assisting*). This graph shows that temperature is boosted strongly when the radiation parameter is increased. Rd features in the augmented thermal diffusion term, $(1 + Rd)\theta''$ in the energy Eqn. (24). $Rd = \frac{16\sigma T_\infty^3}{3k\kappa}$ and expresses the relative contribution of thermal radiation to thermal conduction heat transfer. For $Rd = 0$ radiative flux effects vanish and temperature is minimized (purely conductive heat transfer). With increasing Rd , the optically thick nanofluid is energized by thermal radiation and this induces significant heating, leading also to a growth in thermal boundary layer thickness. As with other temperature graphs, higher temperature magnitudes are computed for $U_e < 0$ (*opposing electrical field*) compared with $U_e > 0$ (*assisting electrical field*), again emphasizing that the direction of applied axial electrical field has a strong effect on temperature distributions. An increase in the Eckert number (Ec) as observed in Fig. 3(h) modifies both the viscous heating and Joule heating terms and elevates the temperature magnitudes since more mechanical energy is converted to thermal energy in the regime. Higher temperatures correspond to $U_e < 0$ (*opposing electrical field*) and lower temperatures for $U_e > 0$ (*assisting*

electrical field). The Eckert number describes the relationship between kinetic energy and enthalpy difference in the boundary layer. Work done against viscous forces results in conversion of fluid kinetic energy to internal energy. Increased kinetic energy produces greater molecular vibration, leading to more collisions between molecules and heats the regime. Neglecting dissipation effects ($Ec = 0$) in mathematical models therefore leads to an under-prediction in temperatures and a lower estimation of thermal boundary layer thickness. The effect of heat sink ($Q < 0$) or heat source ($Q > 0$) parameters on the temperature profile of nanoparticles is shown in Fig. 3(i) for both electrical field cases. The nanoparticles and base fluid become hotter as the strength of the heat source ($Q > 0$) increases and the heat generated increases the thickness of the boundary layer. On the other hand, the nanoparticles and base fluid become cooler when the strength of the heat sink ($Q < 0$) increases and this manifests in a depletion in thermal boundary layer thickness, for both $U_e < 0$ (*opposing electrical field*) and $U_e > 0$ (*assisting electrical field*) cases, although as noted earlier, the former achieves higher temperatures.

Figures 4 - 9 show the influence of selected parameters on the concentration of nanoparticles (φ) and the concentration of microorganisms (motile number density), (χ) through the boundary layer domain with constrained values of other parameters. The impact of electroosmotic parameter (κ) on nanoparticle concentration and microorganism concentration are shown in Fig. 4(a-b). Evidently the concentration of nanoparticles increases with the increase in the value of the electroosmosis parameter (see Fig. 4(a)). The opposite behavior is observed in the profile of the concentration of microorganisms (Fig. 4(b)). A decrease in electrical double layer (EDL) thickness therefore produces a strong accentuation in nanoparticle concentrations whereas it suppresses micro-organism concentrations. The absence of electroosmotic effects corresponds to (κ) which decouples the electrical potential equation (27) from the primary momentum eqn. (22) and therefore all other conservation equations. Nanoparticle concentration boundary layer thickness is therefore enhanced with increasing electroosmotic parameter (κ) or decreasing EDL thickness whereas the converse behavior is induced in the motile gyrotactic micro-organism species boundary layer thickness. Both nanoparticle and micro-organism concentration fields can therefore be manipulated by the electroosmotic body force in the regime. Fig. 5(a-b) shows the influence of the electric field parameter (U_e) on nanoparticle and micro-organism concentration distributions.

$U_e = \frac{1}{aU_w} U_{HS}$ in which $U_{HS} = -\frac{k_B T_v \epsilon_{eff} \Phi_{\chi}}{\mu_f \bar{z} e}$ is the Helmholtz-Smoluchowski velocity. As

elaborated earlier the case of $U_e < 0$ is associated with aligned axial electrical field whereas the case $U_e > 0$ is connected with reversed axial electrical field. The former produces significantly greater magnitudes in nanoparticle and micro-organism concentrations which is sustained through the boundary layer transverse to the wall. In Fig. 6(a-b), indicate that an increment in tangent hyperbolic power law index parameter n strongly enhances both nanoparticle φ and micro-organism concentrations χ . Stronger pseudoplastic behaviour is therefore assistive to the diffusion of the nanoparticles and the propulsion of gyrotactic micro-organisms, since greater shear-thinning is present. Fig.7(a-b) shows that with an increase in Lewis number (Le) there is a significant suppression in both nanoparticle concentration (φ) and microorganism concentration (χ). $Le = \frac{\alpha}{D_B}$ and expresses the ratio of thermal diffusivity (α) to the nanoparticle Brownian diffusion coefficient (D_B). It is distinct from the bioconvection lewis number, $Lb = \frac{v_f}{D_m}$, which expresses the ratio of momentum diffusivity (v_f) to microorganism diffusivity (D_m). Le features only in the nanoparticle concentration boundary layer Eqn. (25) in the terms, $+Le Pr(f + g) \varphi'$ and $-Le Pr \Omega_c ((f' + g')(f + g)\varphi' + (f + g)^2\varphi'')$. When Le is increased, the diffusivity of the nanoparticles decreases and this inhibits diffusion in the boundary layer leading to a depletion in nanoparticle concentration (Fig. 7a), a pattern which is maintained throughout the domain at all values of transverse coordinate, η . Similarly, via coupling of the micro-organism concentration Eqn. (26) to the nanoparticle conservation Eqn. (25), via the term, $-Pe(\chi' \varphi' + (\Omega + \chi)\varphi'')$, the micro-organism concentration is also indirectly affected strongly and is depleted. Motile micro-organism boundary layer thickness is therefore reduced. Significant control of both nanoparticle and gyrotactic micro-organism transport is therefore achieved via modification in only the Lewis number, Le . Fig. 8(a-b) shows that with elevation in Eckert number (Ec) there is a weak reduction in concentration of nanoparticles whereas there is a more significant depletion in concentration of microorganisms. The self-propelling micro-organism concentration is also more substantially influenced for a greater distance into the boundary layer transverse to the wall, whereas the nanoparticle diffusion modification is localized near the wall. Greater sensitivity of the self-propelling micro-organisms is therefore computed to viscous dissipation and Joule heating effects compared with nanoparticles. Fig. 9(a-b), shows that with increment in bioconvection Péclet number (Pe), there is a minor decrease in nanoparticle concentration, φ whereas a substantial decrement in micro-organism concentration χ is computed. An increase in Pe directly strongly accentuates the

$-Pe(\chi'\varphi' + (\Omega + \chi)\varphi'')$ terms in the micro-organism species boundary layer Eqn. (26) but does not directly modify the nanoparticle concentration since Pe is not present in the nanoparticle species conservation Eqn. (25). Since $Pe = \frac{bW_c}{D_m}$, therefore increment in Pe implies a reduction in microorganism diffusivity (D_m) for a fixed swimming speed, W_c and chemotaxis constant, b . This will strongly damp the self-propulsion of micro-organisms but will only weakly decrease nanoparticle concentrations via coupling of the respective concentration equations. A trivial decrease in nanoparticle concentration boundary layer thickness will therefore be induced with higher bioconvection bioconvection Péclet number (Pe), whereas a prominent depletion in micro-organism species boundary layer thickness will be produced.

MATLAB bvp4c numerical results for local Sherwood number $-\varphi(\eta)$ and local density number of microorganisms $-\chi(\eta)$ as a function of several selected nanoscale, rheological, electrical, magnetic, non-Fourier, non-Fickian and micro-organism diffusivity parameters i.e. Nt , Nb , n , We_1 , κ , M , Ω_C , Ω_T and Pe are provided in **Table-2**. It is apparent that $-\varphi(\eta)$ and $-\chi(\eta)$ decrease with increment in Nb , We_1 , Ω_C and Ω_T whereas they both increase with elevation in Nt , n , κ and M . The local Sherwood number $-\varphi(\eta)$ and local density number of microorganisms $-\chi(\eta)$ are opposite in nature for larger values of bioconvection Péclet number, Pe . The Peclet number quantifies the relative significance of advection and diffusion, with a high value indicating an advectively dominated distribution and a small value indicating a diffuse flow.

6. CONCLUSIONS

As a simulation of rheological electro-conductive ionic nano-bio-coating flow processing, a mathematical model for laminar, steady, incompressible bioconvection flow of a tangential hyperbolic (non-Newtonian) nanofluid from a bi-directional stretching surface under mutually orthogonal electrical and magnetic fields has been presented. Nonlinear thermal radiation, Joule heating and heat source/sink effects have been included. The transformed, non-dimensional nonlinear ordinary differential boundary value problem has been solved numerically with an efficient numerical Lobatto - IIIa collocation method available in the MATLAB bvp4c shooting solver. The principal findings of the present study which has considered a fixed stretching rate ratio, may be summarized as follows:

- The axial velocity decreases with increment in tangent hyperbolic rheological parameters (We_I & n) for both cases of $U_e < 0$ (aligned electrical field) and $U_e > 0$ (reversed electrical field).
- Increment in the Eckert number, which increases both viscous and Houle heating effects, leads to an increase in the axial fluid velocity. Elevation of the mixed convection parameter (λ) and buoyancy ratio parameter (Nr), which decreases the velocity of the fluid in the axial direction, increases the axial velocity magnitudes.
- Both the number of magnetic interactions and the electroosmosis parameter increase the temperature and the thickness of the thermal boundary layer.
- The nanoparticle species concentration and associated boundary layer thickness increases with a decrease in the electric field parameter (U_e), Lewis number (Le) and Eckert number (Ec), whereas it increases with an increment in rheological parameter (n) and electroosmosis parameter (κ) i.e. inverse electrical double layer (EDL) thickness.
- The density number (concentration) of motile microorganisms is a decreasing function of the electroosmosis parameter, the electric field parameter, the bioconvection Péclet number and the ordinary Lewis number.
- The local Sherwood number decreases while the local density of motile microorganisms increases as a function of bioconvection Péclet number.
- The local Sherwood number goes down and the local density of moving microorganisms goes up as a function of the bioconvection Péclet number.
- The local density of the motile microorganisms is a decreasing function of the rheological parameters (We_I & n) of tangent hyperbolic nanofluids and the non-Fourier thermal and non-Fickian concentration (solutal) relaxation parameters (Ω_T, Ω_C).
- Increasing Eckert number reduces motile micro-organism density whereas it elevates temperatures.

The present study has revealed some interesting characteristics of advanced functional electromagnetic nanofluid coating flows with non-Fourier and non-Fickian effects. However future works may generalize the model to consider the following:

- Homogeneous-heterogeneous chemical reactions may be considered via appropriate formulations.

- Other non-Newtonian fluid models can also be explored such as the Jeffreys viscoelastic model [64].
- The Buongiorno nanoscale model may be replaced by the Tiwari-Das model, which allows a wide range of combinations of metallic and carbon-based nanoparticles and base fluids to be studied.

Conflict of interest statement: On behalf of all authors, the corresponding author states that there is no conflict of interest.

REFERENCES

1. R. Zhu *et al.*, Anisotropic magnetic liquid metal film for wearable wireless electromagnetic sensing and smart electromagnetic interference shielding, *Nano Energy*, 92, 106700 (2022).
2. Z. Ding *et al.*, Facile fabrication of superhydrophobic polysiloxane/magnetite nanocomposite coatings with electromagnetic shielding property, *Journal of Coatings Technology and Research* volume 8, Article number: 757 (2011).
3. Gass, J, Poddar, P, Almand, J, Srinath, S, Srikanth, H, Superparamagnetic polymer nanocomposites with uniform Fe₃O₄ nanoparticle dispersions. *Adv. Funct. Mater.*, 16 71–75 (2006).
4. Small, AC, Johnston, JH, Novel hybrid materials of magnetic nanoparticles and cellulose fibers. *J. Colloid Interf. Sci.*, 331 122–126 (2009).
5. D.J. Walton, Electrically conducting polymers, *Materials & Design*, 11, 142-152 (1990).
6. D.S. Park and K.S. Park, Optimal functional surface coating considering internal flow behavior of viscous liquids driven by vertical ultrasonic waves, *Results in Physics*, 25, 104255 (2021).
7. S. J. Weinstein and K. J. Ruschak, Coating Flows, *Annual Review of Fluid Mechanics*, 36: 29-53 (2004).
8. Riley, J.J., Gad-el-Hak, M., and Metcalfe, R.W. Compliant coatings, *Ann. Rev. Fluid Mech.* 20, pp. 393-420 (1988).
9. R. Mehmood, Rabil Tabassum, S. Kuharat, O. Anwar Bég and M. Babaie, Thermal slip in oblique radiative nano-polymer gel transport with temperature-dependent viscosity: solar

- collector nanomaterial coating manufacturing simulation, *Arabian J. Science and Engineering*, 44, pages1525–1541 (2019).
10. K. Pattnaik, S. R. Mishra, O. Anwar Bég, U. F. Khan and J.C. Umavathi, Axisymmetric radiative titanium dioxide magnetic nanofluid flow on a stretching cylinder with homogeneous/heterogeneous reactions in Darcy-Forchheimer porous media: *intelligent nanocoating simulation*, *Materials Science and Engineering B* (2021). doi.org/10.1016/j.mseb.2021.115589 (26 pages)
 11. Choi SUS. Enhancing thermal conductivity of fluids with nanoparticle. In: *Development and applications of non-Newtonian flow*, FED-vol. 231/MD-vol. 66. ASME; 1995. p. 99–105.
 12. Lee S, Choi SUS, Li S, Eastman JA. Measuring thermal conductivity of fluids containing oxide nanoparticles. *ASME J. Heat Transfer*, 1999; 121:280.
 13. Eastman JA, Choi SUS, Li S, Yu W, Thompson LJ. Anomalously increased effective thermal conductivity of ethylene glycol-based nanofluids containing copper nanoparticles. *Appl Phys Lett* 2001;78(6):718–20.
 14. Buongiorno J. Convective transport in nanofluids. *ASME J. Heat Transfer* 2006; 128:240–50.
 15. Haddad Z, Nada A, Oztop F, Mataoui A. Natural convection in nanofluids: are the thermophoresis and Brownian motion effect significant in nanofluids heat transfer enhancement? *Int J Therm Sci* 2012; 57:152–62.
 16. Al-Amri F, Muthamilselvan, Stagnation point flow of nanofluid containing micro-organisms, *Case Studies in Thermal Engineering*, 2020, 21, 100656.
 17. Olanrewaju AM, Makinde OD. On boundary layer stagnation point flow of a nanofluid over a permeable flat surface with Newtonian heating. *Chem Eng Commun* 2013; 200:836–52.
 18. Kandasamy R, Muhaimin I, Mohamad R. Thermophoresis and Brownian motion effects on MHD boundary-layer flow of a nanofluid in the presence of thermal stratification due to solar radiation. *Int J Mech Sci* 2013; 70:146–54.
 19. Ibrahim W, Shanker B. MHD boundary layer flow and heat transfer of a nanofluid past a permeable stretching sheet with velocity, thermal and solutal slip boundary conditions. *Comput Fluids*, 2013; 75:1–10.

20. H. Bruus, *Theoretical Microfluidics*, Oxford Master Series in Condensed Matter Physics, Oxford University Press, Oxford, UK, 2008.
21. F.F. Reuss, Sur un nouvel effet de l'électricité galvanique, *Memoires de la Societe Imperiale des Naturalistes de Moscou* vol.2, pp.327–337, 1809.
22. H. Helmholtz, Über den Einfluss der elektrischen Grenzschichten bei galvanischer Spannung und der durch Wasserströmung erzeugten Potentialdifferenz, *Ann.* vol.7, p.337, 1879.
23. M. von Smoluchowski, Versuch einer mathematischen Theorie der Koagulationskinetik kolloid Lösungen, *Z. Phys. Chem.* vol. 92, pp. 129–135, 1917.
24. D. Burgreen, F.R. Nakache, Electrokinetic flow in ultrafine capillary slits, *J. Phys. Chem.* vol. 68, pp. 1084–1091, 1964.
25. J.E. Melanson *et al.*, Dynamic capillary coatings for electroosmotic flow control in capillary electrophoresis, *TrAC Trends in Analytical Chemistry*, 20, 365-374 (2001).
26. S. Bekri *et al.*, Polyelectrolyte multilayer coatings for the separation of proteins by capillary electrophoresis: Influence of polyelectrolyte nature and multilayer crosslinking, *J. Chromatography A*, 1399, 80-87 (2015).
27. R. Qiao, Control of electroosmotic flow by polymer coating: effects of the electrical double layer, *Langmuir* 2006, 22, 16, 7096–7100.
28. O. A. Hickey *et al.*, Influence of charged polymer coatings on electro-osmotic flow: molecular dynamics simulations. *Macromolecules* 2011, 44 (23), 9455-9463.
29. L. Li, Qianqian Cao, Hao Liu, Zhiqing Gu, Ying Yu, Fengli Huang, Chuncheng Zuo. Transport of polymer-modified nanoparticles in nanochannels coated with polymers. *RSC Advances* 2019, 9 (67), 38944-38951.
30. Q. Cao, Chuncheng Zuo, Lujuan Li, Yang Yang, Nan Li. Controlling electroosmotic flow by polymer coating: a dissipative particle dynamics study. *Microfluidics and Nanofluidics* 2011, 10 (5), 977-990.
31. J.R. Platt, Bioconvection patterns in cultures of free-swimming organisms. *Science*. 1961; 133:1766–7.
32. S. Ghorai and N.A. Hill, Wavelengths of gyrotactic plumes in bioconvection, *Bull Math Biol.*, 62(3):429-50 (2000).

33. Y. Ma, Seed coating with beneficial microorganisms for precision agriculture, *Biotechnology Advances*, 37, 107423 (2019).
34. Pedley, T J & Kessler, J O A new continuum model for suspensions of swimming microorganisms. *J Fluid Mech.*, 212, 155–182 (1990).
35. A. Guimarães *et al.*, Edible films and coatings as carriers of living microorganisms: a new strategy towards biopreservation and healthier foods, *Comprehensive Reviews in Food Science and Food Safety*, 17, 594-614 (2018).
36. M.C. Flickinger and O.I. Bernal, Biocoatings: challenges to expanding the functionality of waterborne latex coatings by incorporating concentrated living microorganisms, *Journal of Coatings Technology and Research*, 14, 791–808 (2017).
37. Zhao, M., Xiao, Y., and Wang, S. Linear stability of thermal-bioconvection in a suspension of gyrotactic micro-organisms, *International Journal of Heat and Mass Transfer*, 126, pp. 95{102 (2018).
38. Aneja, Sapna Sharma, S. Kuharat and O. Anwar Bég, Computation of electroconductive gyrotactic bioconvection under nonuniform magnetic field: Simulation of smart biopolymer coatings for solar energy, *Int. J. Modern Physics B*, 33, 2050028 (22 pages). (2020).
39. N. Islam Nima, M. Ferdows, O. Anwar Bég, S. Kuharat and A. Nakayama, Biomathematical model for gyrotactic free-forced bioconvection with oxygen diffusion in near-wall transport within a porous medium fuel cell, *Int. J Biomathematics* (2020). 2050026 (25 pages). DOI: 10.1142/S1793524520500266
40. Sanches L.M., Petri D.F.S., de Melo Carrasco L.D., Carmona-Ribeiro A.M. The antimicrobial activity of free and immobilized poly (diallyldimethylammonium) chloride in nanoparticles of poly (methylmethacrylate), *J. Nanobiotechnol.*, 2015; 13:58. doi: 10.1186/s12951-015-0123-3
41. H. Bahrulolum *et al.*, Green synthesis of metal nanoparticles using microorganisms and their application in the agrifood sector, *J. Nanobiotechnology*, 19, Article number: 86 (2021)
42. Shankar SS, Rai A, Ahmad A, Sastry M. Rapid synthesis of Au, Ag, and bimetallic Au core–Ag shell nanoparticles using Neem (*Azadirachta indica*) leaf broth. *J Colloid Interface Sci.* 2004;275(2):496–502.

43. A.V. Kuznetsov, The onset of nanofluid bioconvection in a suspension containing both nanoparticles and gyrotactic microorganisms, *International Communications in Heat and Mass Transfer*, 37 (10) (2010) 1421–1425.
44. A. Kuznetsov, A. V., Nanofluid bioconvection in water-based suspensions containing nanoparticles and oxytactic microorganisms: oscillatory instability, *Nanoscale Res. Lett.* 6 (1) (2011) 100.
45. A.V. Kuznetsov, Non-oscillatory and oscillatory nanofluid bio-thermal convection in a horizontal layer of finite depth, *European Journal of Mechanics-B/Fluids* 30 (2) (2011) 156–165.
46. O. Anwar Bég, M. Faisal Md Basir, M.J. Uddin, and A. I. Md. Ismail, Numerical study of slip effects on asymmetric bioconvective nanofluid flow in a porous microchannel with an expanding/contracting upper wall using Buongiorno's model, *J. Mechanics in Medicine and Biology*, 17 (5) 1750059 (28 pages) (2017).
47. O. Anwar Bég, Nonlinear multi-physical laminar nanofluid bioconvection flows: Models and computation, A. Sohail, Z. Li (Eds.): *Computational Approaches in Biomedical Nano-Engineering*, Wiley, Chapter 5, 113-145 (2018).
48. Qin, Yinghong. "Simulation of MHD impact on nanomaterial irreversibility and convective transportation through a chamber." *Applied Nanoscience* (2021): 1-14.
49. Bellila, Abdelkader, Mohammed El Hadi Attia, A. E. Kabeel, Mohamed Abdelgaied, K. Harby, and Jihen Soli. Productivity enhancement of hemispherical solar still using Al₂O₃-water-based nanofluid and cooling the glass cover. *Applied Nanoscience* 11, no. 4 (2021): 1127-1139.
50. Sen, Srijita, Trishna Bal, and Aditya Dev Rajora. "Green nanofiber mat from HLM–PVA–Pectin (Hibiscus leaves mucilage–polyvinyl alcohol–pectin) polymeric blend using electrospinning technique as a novel material in wound-healing process." *Applied Nanoscience* (2022): 1-14.
51. Waqas, H., Khan, S. U., Hassan, M., Bhatti, M. M., & Imran, M. (2019). Analysis on the bioconvection flow of modified second-grade nanofluid containing gyrotactic microorganisms and nanoparticles. *Journal of Molecular Liquids*, 291, 111231.

52. Khan, S. U., Waqas, H., Bhatti, M. M., & Imran, M. (2020). Bioconvection in the rheology of magnetized couple stress nanofluid featuring activation energy and Wu's slip. *Journal of Non-Equilibrium Thermodynamics*, 45(1), 81-95.
53. Zaman S, Gul M. Magnetohydrodynamic bioconvective flow of Williamson nanofluid containing gyrotactic microorganisms subjected to thermal radiation and Newtonian conditions. *Int J Ambient Energy*. 2019; 479:22–8.
54. H. Thameem Basha, R. Sivaraj, V. R. Prasad, O. Anwar Bég, Entropy generation of tangent hyperbolic nanofluid flow over a circular cylinder in the presence of nonlinear Boussinesq approximation: A non-similar solution, *J. Thermal Analysis and Calorimetry* (2020). <https://doi.org/10.1007/s10973-020-09981-5>
55. Y. Wang, H. Waqas, M. Tahir, M. Imran, C.Y. Jung, Effective Prandtl aspects on bioconvective thermally developed magnetized tangent hyperbolic nanofluid with gyrotactic microorganisms and second order velocity slip, *IEEE Access* 7 (2019) 130008–130023.
56. G. Kumaran, R Sivaraj, V. Ramachandra Prasad, O. Anwar Bég, Numerical study of axisymmetric magneto-gyrotactic bioconvection in non-Fourier tangent hyperbolic nanofunctional reactive coating flow of a cylindrical body in porous media, *European Physical Journal Plus*, 136, 1107 (2021). (32 pages) <https://doi.org/10.1140/epjp/s13360-021-02099-z>
57. A. Shafiq, Z. Hammouch, T.N. Sindhu, Bioconvective MHD flow of tangent hyperbolic nanofluid with newtonian heating, *Int. J. Mech. Sci.* 133 (2017) 759–766.
58. A.A. Tracton (Editor), *Coatings Technology Handbook*, CRC Press, Florida (2005).
59. Wang, C. Y. The three-dimensional flow due to a stretching sheet. *Physics of Fluids*, 27, 1915–1917,(1984).
60. A. Shahid, M. M. Bhatti, O. Anwar Bég, I. L. Animasaun and K. Javid, Spectral computation of reactive bi-directional hydromagnetic non-Newtonian convection flow from a stretching upper parabolic surface in non-Darcy porous medium, *Int. J. Modern Physics B* (2021). 2150294 (26 pages). DOI: 10.1142/S0217979221502945
61. N.A. Amirsom, M. J. Uddin, M.F.M.Basir, A. I. Ismail, O. Anwar Bég and Ali Kadir, Three-dimensional bioconvection nanofluid flow from a bi-axial stretching sheet with anisotropic slip, thermal jump and mass slip effects, *Sains Malaysiana* 48(5)(2019): 1137–1149.

62. J. Liu et al., Functional hydrogel coatings, *Nat Sci Rev.*; 8(2) (2021). doi: [10.1093/nsr/nwaa254](https://doi.org/10.1093/nsr/nwaa254)
63. Z. Iqbal et al., The mechanical aspects of bidirectional stretching on thermal performance in Burgers nanofluid flow subject to ohmic heating and chemical reaction, *Proceedings of the Institution of Mechanical Engineers, Part E: Journal of Process Mechanical Engineering* (2021). doi.org/10.1177/0954408921999613
64. D. A. Edwards, Non-Fickian diffusion in thin polymer films, *Journal of Polymer Science: Part B: Polymer Physics*, 34, 981-997 (1996).
65. T. Hayat, S.A. Shehzad, A. Alsaedi, Three-dimensional stretched flow of Jeffery fluid with variable thermal conductivity and thermal radiation, *Appl. Math. Mech. – Engl. Ed.*, 34 (7), 823-832, (2013).
66. I. Sadham Hussain, D. Prakash, S. Kumar, M. Muthamilselvan, Bioconvection of nanofluid flow in a thin moving needle in the presence of activation energy with surface temperature boundary conditions, *Proc I Mech E Part E: J Process Mechanical Engineering*, 2021 <https://doi.org/10.1177/09544089211053969>.
67. M. Muthtamilselvan, S. Suganya, Q.M. Al-Mdallal, Stagnation-point flow of the williamson nanofluid containing gyrotactic micro-organisms. *Proc. Natl. Acad. Sci., India, Sect. A Phys. Sci.* **91**, 633–648 (2021).